Galaxy And Mass Assembly (GAMA): Data Release 4 and the $z < 0.1$ total and $z < 0.08$ morphological galaxy stellar mass functions

Simon P. Driver,[1]★ Sabine Bellstedt,[1] Aaron S. G. Robotham,[1] Ivan K. Baldry,[2] Luke J. Davies,[1] Jochen Liske,[3] Danail Obreschkow,[1] Edward N. Taylor,[4] Angus H. Wright,[5] Mehmet Alpaslan,[6] Steven P. Bamford,[7] Amanda E. Bauer,[8] Joss Bland-Hawthorn,[9] Maciej Bilicki,[10] Matías Bravo,[1] Sarah Brough,[11] Sarah Casura,[3] Michelle E. Cluver,[4,12] Matthew Colless,[13] Christopher J. Conselice,[14] Scott M. Croom,[9] Jelte de Jong,[15,16] Franceso D'Eugenio,[17,18] Roberto De Propris,[19] Burak Dogruel,[4] Michael J. Drinkwater,[20] Andrej Dvornik,[5] Daniel J. Farrow,[21] Carlos S. Frenk,[22] Benjamin Giblin,[23] Alister W. Graham,[4] Meiert W. Grootes,[24] Madusha L. P. Gunawardhana,[15] Abdolhosein Hashemizadeh,[1] Boris Häußler,[25] Catherine Heymans,[5,23] Hendrik Hildebrandt,[5] Benne W. Holwerda,[26] Andrew M. Hopkins,[27] Tom H. Jarrett,[28] D. Heath Jones,[29] Lee S. Kelvin,[30] Soheil Koushan,[1] Konrad Kuijken,[15] Maritza A. Lara-López,[31] Rebecca Lange,[32] Ángel R. López-Sánchez,[27] Jon Loveday,[33] Smriti Mahajan,[34] Martin Meyer,[1] Amanda J. Moffett,[35] Nicola R. Napolitano,[36] Peder Norberg,[22] Matt S. Owers,[37,38] Mario Radovich,[39] Mojtaba Raouf,[15] John A. Peacock,[23] Steven Phillipps,[40] Kevin A. Pimbblet,[41] Cristina Popescu,[42] Khaled Said,[20] Anne E. Sansom,[42] Mark Seibert,[43] Will J. Sutherland,[44] Jessica E. Thorne,[1] Richard J. Tuffs,[45] Ryan Turner,[1,4] Arjen van der Wel,[18] Eelco van Kampen[46] and Steve M. Wilkins[33]

Affiliations are listed at the end of the paper

ABSTRACT

In Galaxy And Mass Assembly Data Release 4 (GAMA DR4), we make available our full spectroscopic redshift sample. This includes 248 682 galaxy spectra, and, in combination with earlier surveys, results in 330 542 redshifts across five sky regions covering ~250 deg^2. The redshift density, is the highest available over such a sustained area, has exceptionally high completeness (95 per cent to $r_{\rm KiDS} = 19.65$ mag), and is well-suited for the study of galaxy mergers, galaxy groups, and the low redshift ($z < 0.25$) galaxy population. DR4 includes 32 value-added tables or Data Management Units (DMUs) that provide a number of measured and derived data products including *GALEX*, ESO KiDS, ESO VIKING, *WISE*, and *Herschel* Space Observatory imaging. Within this release, we provide visual morphologies for 15 330 galaxies to $z < 0.08$, photometric redshift estimates for all 18 million objects to $r_{\rm KiDS} \sim 25$ mag, and stellar velocity dispersions for 111 830 galaxies. We conclude by deriving the total galaxy stellar mass function (GSMF) and its sub-division by morphological class (elliptical, compact-bulge and disc, diffuse-bulge and disc, and disc only). This extends our previous measurement of the total GSMF down to $10^{6.75}\,\mathrm{M}_\odot\,h_{70}^{-2}$ and we find a total stellar mass density of $\rho_* = (2.97 \pm 0.04) \times 10^8\,\mathrm{M}_\odot\,h_{70}\,\mathrm{Mpc}^{-3}$ or $\Omega_* = (2.17 \pm 0.03) \times 10^{-3}\,h_{70}^{-1}$. We conclude that at $z < 0.1$, the Universe has converted 4.9 ± 0.1 per cent of the baryonic mass implied by big bang Nucleosynthesis into stars that are gravitationally bound within the galaxy population.

Key words: catalogues – surveys – galaxies: distances and redshift – galaxies: fundamental parameters – galaxies: luminosity function, mass function – cosmological parameters.

1 INTRODUCTION

Spectroscopic surveys of galaxies are one of the mainstays of observational extragalactic astronomy. These *redshift surveys* started in the 1980s with the Harvard Center for Astrophysics survey led by John Huchra and Margaret Geller (Huchra et al. 1983; de Lapparent,

★ E-mail: simon.driver@uwa.edu.au

Geller & Huchra 1986; Geller & Huchra 1989). This continued with numerous shallow and medium-deep surveys conducted through the 1980s and 1990s, operating mainly on the new 4-m class telescopes, e.g. *Stromlo-APM Redshift Survey* (Loveday et al. 1992); *Durham-UKST Redshift Survey* (Ratcliffe et al. 1996); *Las Campanas Redshift Survey* (Shectman et al. 1996); *ESO slice Project* (Vettolani et al. 1997); *Southern Sky Redshift Survey* (da Costa et al. 1998); *Canadian Network for Cosmology* (Yee et al. 2000), and many more.

In the period leading into the millennium, the subject underwent an 'industrial revolution' through the advent of wide-area multiplexed fibre-fed systems, as used by the *2-degree-Field Galaxy Redshift Survey* (2dFGRS) on the Anglo-Australian Telescope at Siding Spring Observatory in Australia (Colless et al. 2001), and the *Sloan Digital Sky Survey* at Apache Point Observatory in New Mexico, USA (York et al. 2000). These two surveys provided ∼250 000 and over 1 million redshifts, respectively.

Both the 2dFGRS and SDSS surveys based their input catalogues on flux limited samples with minimal pre-selection other than stringent star-galaxy classification criteria, see for example the SDSS selection described in Strauss et al. (2002). Both surveys strove to pursue complete flux-limited samples with relatively high spectroscopic completeness (>80 per cent).

The SDSS survey, in particular, not only advanced the field through the provision of redshifts, but through the release of moderate signal-to-noise spectra (S/N ∼ 5–30), and a dedicated CCD based imaging survey conducted in multiple *ugriz* bandpasses across ∼8000 deg² of the Northern and Equatorial sky (Stoughton et al. 2002). SDSS has continued since this time, diversifying into more focused and niche sub-areas (i.e. SDSS II, Frieman et al. 2008; SDSS III, Eisenstein et al. 2011; SDSS IV, Blanton et al. 2017; SDSS V, commencing in 2021, see Kollmeier et al. 2017 and also http://www.sdss5.org).

Today SDSS remains the preeminent low-*z* spectroscopic survey, responsible for transforming our understanding of the nearby extragalactic sky. While part of the capacity to transform came from the scale, scope and quality of the data, this was magnified by the manner in which the data were made available. As of today, there have been 16 SDSS Public data releases (Ahumada et al. 2020), as well as the efforts of the many who provided derived data products in an Open Source fashion suitable for immediate science e.g. Kauffmann et al. (2003), Brinchmann et al. (2004), Tremonti et al. (2004), Blanton et al. (2005), Simard et al. (2011), and many more.

Since the 2dFGRS and SDSS, and post millennium, there has been a bifurcation in the design and implementation of redshift surveys. One branch has pursued complex target selections, usually colour and/or photometric-redshift based, to maximize survey efficiency for constraining cosmological parameters. This essentially trades completeness for sky-coverage, e.g. the Australian-led *WiggleZ* (Drinkwater et al. 2010) and the US-led *Baryon Oscillation Spectroscopic Survey* (an SDSS extension: Dawson et al. 2013). While these surveys do remain useful for some galaxy population science (e.g. Thomas et al. 2013), the more complex selection and sub-sampling does render some science cases unviable. Obvious examples include the study of merger rates via close dynamical pairs, group finding, and the low-mass end of the galaxy stellar mass function (GSMF), all areas where high-completeness is paramount.

The second branch in the bifurcation followed the path of conducting high-density high-completeness surveys often over more modest regions of sky, with the exception of the very local hemispheric surveys, and with a greater focus on complementary panchromatic data, e.g. *the Millennium Galaxy Catalogue* (Liske et al. 2003); *the 6-degree-Field Galaxy Survey* (6dFGS; Jones et al. 2009); *the Galaxy And Mass Assembly survey* (GAMA; Driver et al. 2011);

and *the Smithsonian Hectospec Lensing Survey* (Geller et al. 2016). These surveys also built on the multiwavelength direction started by SDSS, and in particular capitalized on the available UV (via *GALEX*) and near-infrared (via 2MASS, UKIRT, VISTA, and *WISE*) data. Through collaboration with the *Herschel*-ATLAS survey (Eales et al. 2010), the wavelength coverage of GAMA was extended into the far-IR and now spans 0.15–500 μm (Driver et al. 2016). These surveys, while optimized for galaxy population studies, are sub-optimal for cosmology due to their limited coverage (Blake et al. 2013). However, we note the ability of the very local hemispheric 6dFGS survey to place significant constraints on the Hubble Constant via the detection and measurement of baryonic acoustic oscillations (Beutler et al. 2011), and GAMA to assist in improving the cosmological constraints from the ESO KiDS weak-lensing survey (e.g. Amon et al. 2018; van Uitert et al. 2018; Spurio Mancini et al. 2019)

With the advent of the 8-m class facilities, spectroscopic surveys were extended out to higher redshift, e.g. *the VLT Very Deep Survey*, (Le Fèvre et al. 2005); the zCOSMOS survey, (Lilly et al. 2007); *the Deep Extragalactic Evolutionary Probe 2*, (Newman et al. 2013), and *the VIMOS Public Extragalactic Redshift Survey*, (Guzzo et al. 2014). Here, completeness is also an issue, as on the whole, these surveys are below 50 per cent redshift completeness (see Davies et al. 2018, fig. 1). However, this is less by design and more imposed by either the difficulty of obtaining redshifts for very distant targets, or the logistical restrictions in using multislit devices. Recently the Deep Extragalactic Visible Legacy Survey (DEVILS; Davies et al. 2018), via stacked long-exposure integrations on the 4-m class Anglo-Australian Telescope, is revisiting notable deep fields (COSMOS, XMMLSS, ECDFs), seeking to raise the spectroscopic completeness to >90 per cent, at intermediate magnitudes (*Y* < 21.0 mag) and depth (*z* < 1).

In the very near future, forthcoming multifibre systems on 4-m (e.g. DESI, DESI Collaboration et al. 2016; 4MOST, de Jong et al. 2019; WEAVE, Dalton et al. 2020), and 8-m (MOONS, Cirasuolo et al. 2020; PFS, Wang et al. 2020) class facilities, will transform the existing low, intermediate, and high-redshift domains taking us from the million galaxy redshift scale and into the tens of millions. In the slightly longer term, the proposed and planned 12-m Mauna Kea Spectroscopic Explorer (MSE), a dedicated optical/near-IR multiplexed spectroscopic facility (McConnachie et al. 2016), will extend this to the hundreds of millions, and is essentially capable of sampling the entire observable Universe at masses $>10^9 \, \mathrm{M_\odot} \, h_{70}^{-2}$ since $z \approx 5$. Also notable are the forthcoming European Space Agency Euclid (Laureijs et al. 2011) and NASA SPHEREx (Crill et al. 2020) missions that will survey very large samples within specific high or low redshift windows at low wavelength resolution with grism or linear variable filters, respectively.

In parallel to the progression of spectroscopic survey campaigns, has been the rise of broad-band photometric redshift techniques (see for example the comparison of methods reported in Abdalla et al. 2011), and the narrow-band filter surveys that define the middle ground, e.g. COMBO17, (Wolf et al. 2003); COSMOS, (Laigle et al. 2016); ALHAMBRA, (Molino et al. 2014); J-PAS (Benitez et al. 2014); PAUS (Eriksen et al. 2019); and OTELO (Bongiovanni et al. 2019). For many purposes, photometric redshifts are sufficient, but once again for merger, group, and very low redshift (*z* < 0.1) science, the traditional photometric surveys struggle with velocity resolutions typically at ∼10 000 km s⁻¹ (broad-band) to ∼1000 km s⁻¹ (narrow-band) compared to the typical galaxy pairwise velocity of 200–600 km s⁻¹ (Loveday et al. 2018) and typical low-mass group velocity dispersions of <500 km s⁻¹ (Robotham et al. 2011).

The Galaxy And Mass Assembly Survey (GAMA; Driver et al. 2011), commenced in 2008 with the goal of building upon the legacy of the original 2dFGRS and SDSS surveys to produce a *highly complete* redshift survey with *maximal multiwavelength data* (x-ray-to-radio via eROSITA, *GALEX*, VST, VISTA, *WISE*, *Herschel*, ASKAP, and MWA). GAMA data thus far, have been used to explore merger rates (Casteels et al. 2014; De Propris et al. 2014; Robotham et al. 2014; Davies et al. 2015), galaxy groups (Robotham et al. 2011; Khosroshahi et al. 2017; Raouf et al. 2019; Taylor et al. 2020; Raouf et al. 2021), the low-*z* Universe (Gunawardhana et al. 2011; Driver et al. 2012; Kelvin et al. 2012; Loveday et al. 2012; Lara-López et al. 2013; Cluver et al. 2014; Oliva-Altamirano et al. 2014; Lange et al. 2015; Moffett et al. 2016; Beeston et al. 2018; Bellstedt et al. 2020b), and in particular the low-*z* GSMF (Baldry et al. 2012; Moffett et al. 2016; Wright et al. 2017): the benchmark for most numerical simulations.

GAMA extends over five regions of sky covering 250 deg^2, and over the past decade, we have obtained $\sim$230 000 spectroscopic redshift measurements with a median accuracy of $\pm$35 km s^{-1} (Liske et al. 2015), and complementary imaging, either directly or via collaboration, extending from the UV to the far-IR, i.e. 20-band photometry (see Driver et al. 2016) extending from 0.2–500 μm.

To date, there have been three GAMA data releases (Driver et al. 2011; Liske et al. 2015; Baldry et al. 2018), and in this paper, we now provide the fourth (GAMA DR4), which includes all redshifts (including those obtained by GAMA or by other surveys), all spectra, and our revised 20-band UV to far-IR photometry for those galaxies with spectroscopic redshifts (Bellstedt et al. 2020a). In addition, we provide over 30 value added data tables or Data Management Units (DMUs). These consist of many measured (Level 2) and derived quantities (Level 3), created by the GAMA team, providing quality controlled science-ready products to the global community (see http://www.gama-survey.org/dr4/)

The paper concludes with a revised measurement of one of our headline goals, the GSMF and its sub-division by morphological type. It extends our previous estimates from 10^8 M$_\odot$ h_{70}^{-2} to a new lower mass-limit of $10^{6.75}$ M$_\odot$ h_{70}^{-2} at $z < 0.1$.

In Section 2, we incorporate our recent image analysis (Bellstedt et al. 2020a) of the ESO KiDS (Kuijken et al. 2019) and ESO VIKING (Edge et al. 2013) Public Survey data with the GAMA spectroscopic data, and explore our effective redshift completeness for each region and the combined primary regions. In Section 3, we provide new or revised DMUs including photometric redshift estimates for all objects in our revised Input Catalogue, and morphological classifications for all objects with $z < 0.08$ and $r_{\mathrm{KiDSDR4}} < 19.65$ mag. Section 4 describes the contents of Data Release 4. In Section 5, we provide a revised measurement of the GSMF ($z < 0.1$), and its sub-division by morphological type ($z < 0.08$). Finally, in Section 6, we discuss the implication for the cosmic stellar mass density at $z < 0.1$, including a re-normalization from the 230 deg^2 GAMA area to a 5012 deg^2 region of the SDSS area, reducing our cosmic variance uncertainty at $z < 0.1$ from 12 to 6.5 per cent.

We adopt a concordance '737 cosmology', with $(H_0, \Omega_M, \Omega_\Lambda) = (70, 0.3, 0.7)$ throughout, all magnitudes and fluxes are corrected for Galactic extinction, and all magnitudes are reported in the AB system. For all values which are dependent on Hubble's constant, H_0 we include this dependency via $h_{70} = H_0/70$ km s^{-1} Mpc^{-1}.

2 UNIFICATION OF GAMA EQUATORIAL (G09, G12, AND G15) AND 23^h REGIONS (G23)

In this data release, we include a replacement of the original SDSS (equatorial fields) and ESO VLT Survey Telescope (VST; G23) input catalogues, with deeper homogeneous *ugri* imaging from the ESO VST Kilo-Degree Survey (KiDS) Data Release 4 (Kuijken et al. 2019; Bellstedt et al. 2020a). In this section, we introduce the new data, and quantify the implications of replacing our underlying Input Catalogue in terms of revised magnitude limits for a range of desired spectroscopic completeness limits.

2.1 Incorporating Kilo-Degree Survey imaging

The Galaxy And Mass Assembly survey (Driver et al. 2009, 2011) conducted its first spectroscopic observations in 2008 (see Liske et al. 2015). The spectroscopy was based on an initial target catalogue for the three equatorial regions (Baldry et al. 2010) drawn from the 6th data release of the Sloan Digital Sky Survey (Adelman-McCarthy et al. 2008). Later, the survey was extended with an input catalogue for the G02 region created from the CFHT Lensing Survey (CFHTLenS; Erben et al. 2013) and for the G23 region from the ESO VST Kilo-Degree Survey Data Release 1 (de Jong et al. 2015). These optical imaging data, along with the UKIDSS Large Area Survey near-IR data (Lawrence et al. 2007), formed the basis of our input catalogues using angular size and concentration, combined with an additional $(J-K_s)$ colour selection to recoup compact galaxy systems (see full details in Baldry et al. 2010).

The GAMA optical/near-IR input catalogue data were later complemented by UV to far-IR imaging data from *GALEX*, ESO VISTA VIKING, *WISE*, and the *Herschel* Space Observatory, as described in Driver et al. (2016). In particular, the large majority of the *GALEX* data covering the G23 region was acquired in a dedicated observing campaign as part of the All-sky UV Survey Extension, following the hand over of *GALEX* to Caltech and prior to decommissioning. Ultimately, the G02 spectroscopic survey was not completed to its full extent, and all available G02 data were released as part of GAMA DR3 (Baldry et al. 2018).

Recently, we have updated the original equatorial SDSS imaging data with deeper and higher spatial resolution *ugri* observations that extend to $r = 25$ mag, from the European Southern Observatory's VLT Survey Telescope Kilo-Degree Survey Data Release 4 (KiDS; Kuijken et al. 2019). The KiDS data complement the existing panchromatic data from UV to far-IR, providing consistent imaging data to unify the equatorial and G23 regions on to a single photometric and astrometric reference frame in *FUV*, *NUV*, *ugri*, *ZYJHK*, *W*1234, *P*100/160, *S*250/350/500 wavebands. The construction of the KiDS catalogue for GAMA (i.e. GKVINPUTCATV01) resulted in the detection and measurement of over 18-million objects extending to $r \sim 24$ mag and is described in detail in Bellstedt et al. (2020a).

The reanalysis of the FUV-far-IR data used a new source finding algorithm designed for these data, PROFOUND (Robotham et al. 2018), and is based on the precepts of dilated isophotal segments and watershed deblending. This reanalysis included improved star-masking based on GAIA DR2 (Gaia Collaboration et al. 2018), and improved Galactic Extinction corrections based on Planck dust extinction maps (Planck Collaboration XI 2014). A careful verification and reconstruction of all bright and dense regions with multiple abutting segments was conducted, to ensure the integrity of the bright, large, and diffuse galaxies, i.e. those that are well-suited to studies with integral field units (e.g. SAMI, Croom et al. 2021; Hector, Bryant et al. 2020) and/or radio observatories (ASKAP, Hotan et al. 2021; MWA, Tingay et al. 2013; etc).

Most importantly of all, the revised catalogue now allows us to bring together the three equatorial fields and the G23 field with fully consistent and homogeneous photometric measurements from the UV to far-IR using identical facilities to comparable sensitivity limits.
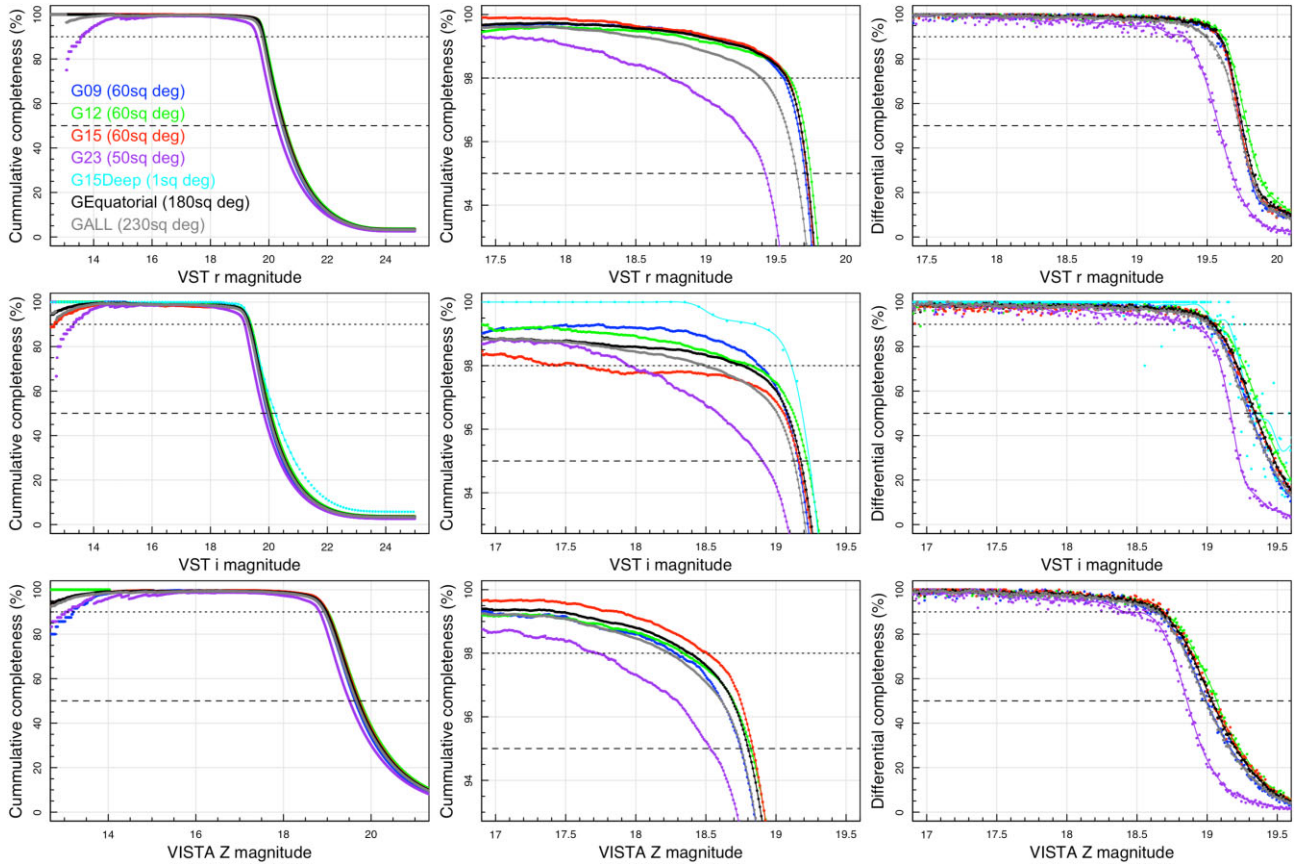
Figure 1. (Left-hand panels) The cumulative spectroscopic completeness of the GAMA survey as a function of limiting VST *r* (upper), VST *i* (middle), and VISTA *Z* (lower) wavebands with the 50 per cent (dashed) and 90 per cent (dotted) lines shown. (Centre panels)A zoom in to the critical turn-over in completeness. The lines now show the 98 and 95 per cent completeness. (Right-hand panels) The differential completeness around the cutout flux limits, the lines show the 50 and 90 per cent limits. See Table 1 for more precise cutoff limits.

2.2 Spectroscopic completeness against KiDS

A key issue raised in 'replacing the tablecloth' (i.e. swapping the SDSS with KiDS photometry), is a change in the spectroscopic completeness profile from one with a sharp spectroscopic selection boundary ($r_{SDSS}^{Petro} < 19.8$ mag in the equatorial fields and $i_{KiDSDR1} < 19.2$ mag in G23), to one with a soft edge. This is because some galaxies with SDSS photometry brighter than our original SDSS flux limit are now found to be fainter in KiDS and vice versa resulting in a less sharp cutoff in spectroscopic completeness. While the KiDS-based catalogues should represent a significant improvement over the original SDSS data, due to the depth of the VST observations, the spectroscopic completeness remains tied to the original SDSS data.

The simplest way to overcome this is to pull back slightly in terms of the completeness limit, and to attempt to identify a revised shallower limit with a spectroscopic completeness comparable to that of the original spectroscopic survey. The advantage is the ability to use the improved photometry without the need to consider complex selection functions, the disadvantage is the inevitable loss of depth (statistical significance), as some fraction of the spectroscopic redshifts are scattered fainter and some larger fraction of sources for which redshifts were not sought are scattered brightwards. For GAMA, the loss of depth is compensated for, if the G23 region can be brought into selection alignment with the equatorial fields, i.e. while the survey depth is slightly diminished (0.15 mag, see Fig. 1 and subsequent discussion), the survey area is increased (by 28 per cent), and the overall cosmic (sample) variance (CV) is reduced by 15 per cent.

In Liske et al. (2015), we reported a combined spectroscopic completeness of 98.48 per cent to $r_{SDSS} = 19.8$ mag in the equatorial fields (G09+G12+G15), 95.5 per cent in the 20 deg² high-completeness portion of the G02 region to $r_{CFHT} = 19.8$ mag, and 94.19 per cent to $i_{KiDSDR1} < 19.2$ mag in the G23 field. Hence we aspire, with the revised photometry, to achieve comparable completeness levels of 95 or 98 per cent.

All G02 data were released in Baldry et al. (2018) and as its panchromatic coverage is quite different, we consider it no further. In Fig. 1, we show the revised completeness of the remaining fields (coloured lines), for the equatorial regions combined (black line), and for all four fields combined (grey lines), as a function of KiDS *r* (top panels), KiDS *i* (centre panels), and VIKING *Z* (lower panels) magnitudes. The left-side and centre-column panels show the cumulative distributions with the central panels representing a zoom in of the left-side panels. The right-side panels show a zoom in of the differential distribution. Table 1 reports the 50, 90, 95, and 98 per cent completeness limits for each of these bands, for each field and for various combinations.

For the remainder of this paper, we now consider the GAMA main survey catalogue (GAMA MS) to be defined by $r_{KiDSDR4} < 19.65$ mag from the combined G09+G12+G15+G23 regions. This contains 205 540 galaxies for which 195 432 have reliable (i.e. *NQ* > 2) redshifts (i.e. 95.1 per cent). GAMA MS+ comprises a further 135 110 redshifts which consist of those galaxies in the G02 region, galaxies fainter than our revised limit, and galaxies on the periphery of the four main survey fields. Fig. 2 shows a cone-plot of the RA

Table 1. The magnitude limits for individual GAMA fields and combinations, for a range of filters and spectroscopic completeness limits. The number of galaxies with spectroscopic redshifts within the associated magnitude limit are shown in brackets.

| Field(s) | Spectroscopic completeness limits: mag (number with reliable spec-z) | | | |
	50 per cent	90 per cent	95 per cent	98 per cent
	$r_{KiDSDR4}$-band magnitude limit to achieve a spec-z completeness of:			
G09	20.45 (58740)	19.80 (53519)	19.71 (51084)	19.55 (43880)
G12	20.55 (68454)	19.85 (61831)	19.75 (58798)	19.60 (51834)
G15	20.52 (65276)	19.81 (58547)	19.72 (56254)	19.58 (50098)
G23	20.28 (41415)	19.59 (37842)	19.42 (33388)	18.74 (16033)
G09+G12+G15	20.51 (192483)	19.82 (173640)	19.72 (165294)	19.58 (146225)
G09+G12+G15+G23	20.46 (233199)	19.77 (210272)	**19.65 (195432)**[a]	19.40 (153601)
	$i_{KiDSDR4}$-band magnitude limit to achieve a spec-z completeness of:			
G09	19.95 (58694)	19.30 (50185)	19.16 (44749)	18.89 (33053)
G12	20.07 (68343)	19.38 (58581)	19.22 (51833)	18.82 (34129)
G15	20.02 (64954)	19.32 (54978)	19.16 (48581)	17.62 (8298)
G23	19.82 (41320)	19.17 (37799)	18.91 (29834)	17.95 (9801)
G15Deep	20.22 (1826)	19.36 (1464)	19.24 (1380)	19.11 (1248)
G09+G12+G15	20.02 (191996)	19.33 (163127)	19.18 (145007)	18.76 (91966)
G09+G12+G15+G23	19.98 (232967)	19.28 (197009)	19.13 (175087)	18.49 (85776)
	Z_{VISTA}-band magnitude limit to achieve a spec-z completeness of:			
G09	19.63 (58477)	18.93 (45812)	18.75 (38268)	18.28 (21214)
G12	19.75 (67714)	19.01 (54536)	18.82 (46162)	18.34 (27062)
G15	19.72 (64617)	19.00 (52161)	18.84 (45712)	18.50 (31654)
G23	19.51 (41091)	18.82 (35221)	18.53 (26449)	17.71 (10008)
G09+G12+G15	19.70 (190736)	18.98 (152305)	18.80 (129629)	18.38 (80050)
G09+G12+G15+G23	19.66 (231471)	18.94 (185366)	18.75 (156176)	18.24 (86546)

Note. [a] Adopted GAMA Data Release 4 Main Survey (GAMA MS).

Table 2. Summary of the VelocityDispersions DMU, including indicative spectral ranges and resolutions for the four spectral data sources.

Data source	Spectral range	Spectral resolution	Num. spectra	Num. galaxies
GAMA	3730–8850 Å	4.4 Å	88 504	85 687
SDSS	3600–10300 Å	3.5 Å	26 818	23 122
2dFGRS	3600–8000 Å	9.0 Å	14 720	13 782
6dFGS	3950–7600 Å	6.4 Å	974	952
Total			131 016	111 830

and lookback-time distribution (orange for GAMA MS and purple for GAMA MS+), along with the SDSS Main Survey (grey), and the ongoing DEVILS survey (blue). These surveys (SDSS, GAMA, and DEVILS) highlight our current *high-completeness* insight into the $z < 1$ Universe.

3 NEW AND UPDATED DATA MANAGEMENT UNITS (DMUS)

3.1 The GAMA DR4 input catalogue v01 and v02

In using the GKVINPUTCATV01 catalogue (Bellstedt et al. 2020a), we identified a minor flaw in our galaxy rebuilding selection. This resulted in 77 large bright galaxies being heavily fragmented and 1 compact group requiring deblending. For the 77 galaxies, these were typically galaxies which intersected with a bright star, and as a consequence were not selected for manual fixing (see Bellstedt et al. 2020a). While unlikely to impact on any statistical analysis, these very nearby large bright galaxies are of particular interest for a number of nearby low redshift follow-on programmes. Hence, we take this opportunity to fix the apertures for these 77 galaxies, and to rerun our measurement and post-processing pipelines for these systems. As part of this process, we removed 687 fragments

associated with these objects, and replaced their photometry with the 77 revised and rebuilt systems to produce GKVINPUTCATV02.

Fig. 3 shows before and after images for two of these bright galaxies. We note that we also revise our far-IR photometry and our SED analysis to produce GKVPROSPECTV02 following the exact processes outlined in Bellstedt et al. (2020a,b). The revised v02 catalogues are made available via GAMA DR4 and the original v01 catalogues are held in the team data base (i.e. they are not included in the GAMA DR4 release). Note that the one blended group (uberID = 215020829601469) we do not directly fix at this stage. However, in Section 5, where we calculate the GSMF we replace this system by a bespoke reanalysis, in which we identify six Elliptical components, and reassign its total stellar mass according to their fractional flux (28, 37, 16, 14, 4, and 1 per cent).

3.2 GAMA G15-deep

As part of the GAMA observing programme (2014 July–Sept), we experimented with pushing to a deeper magnitude limit of $i_{SDSS} <$ 22 mag within a 1 deg² sub-region of the G15 field (218.5 < RA < 219.5, −1.0 < Dec. <0.0). Within this region, we observed 3241 galaxies, and reliable (i.e. $NQ > 2$ with $P(z) > 0.9$) redshifts were obtained using AUTOZ (Baldry et al. 2014) for 736, which
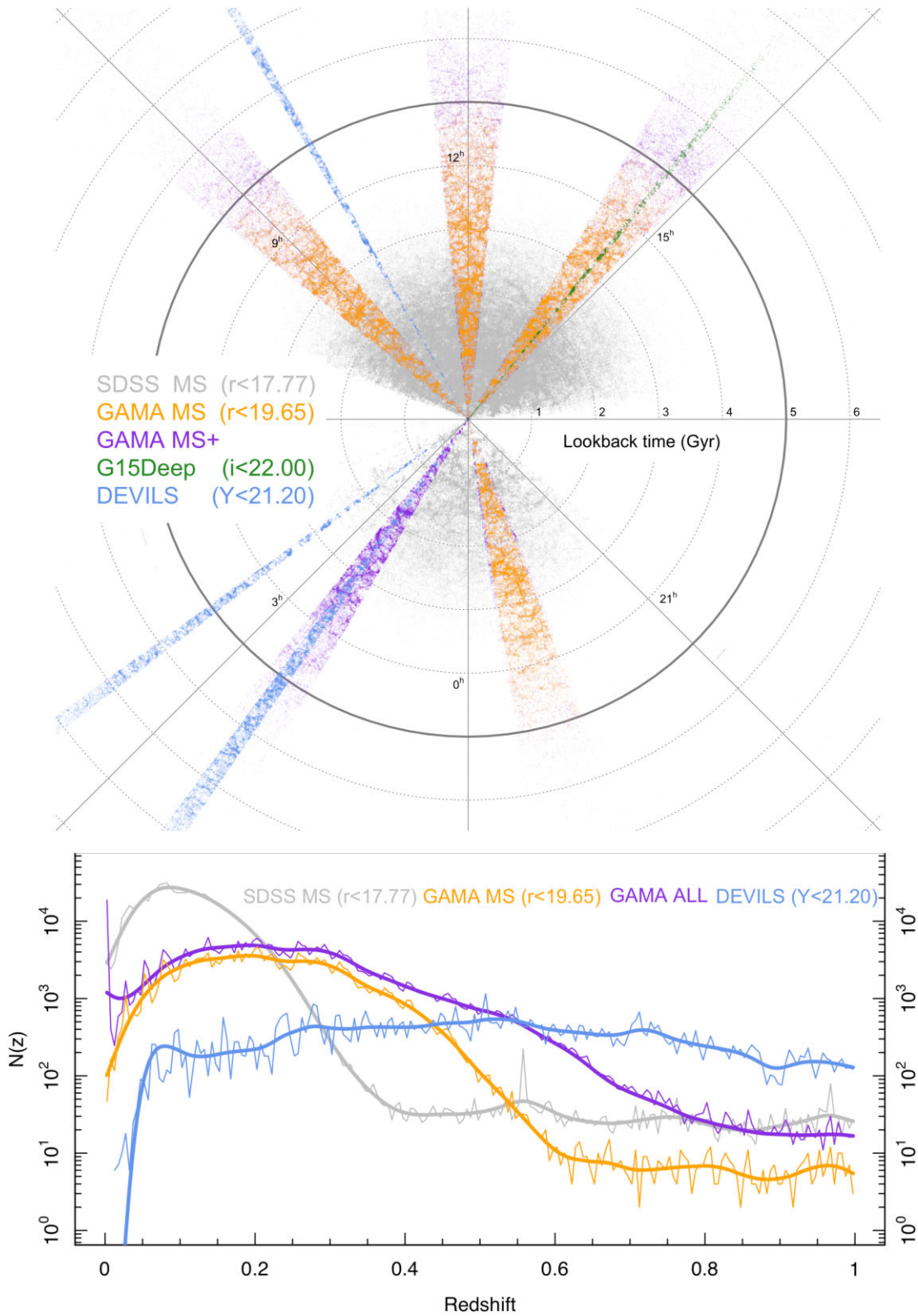
Figure 2. (Upper panel) A cone diagram showing the RA and lookback time distribution of the SDSS, GAMA, and ongoing DEVILS data sets. These are the currently existing high-completeness (∼90 per cent) spectroscopic surveys from which reliable merger rates and group catalogues can be constructed. (Lower panel) The redshift histogram for SDSS main survey, GAMA main survey, GAMA any and DEVILS (as indicated).
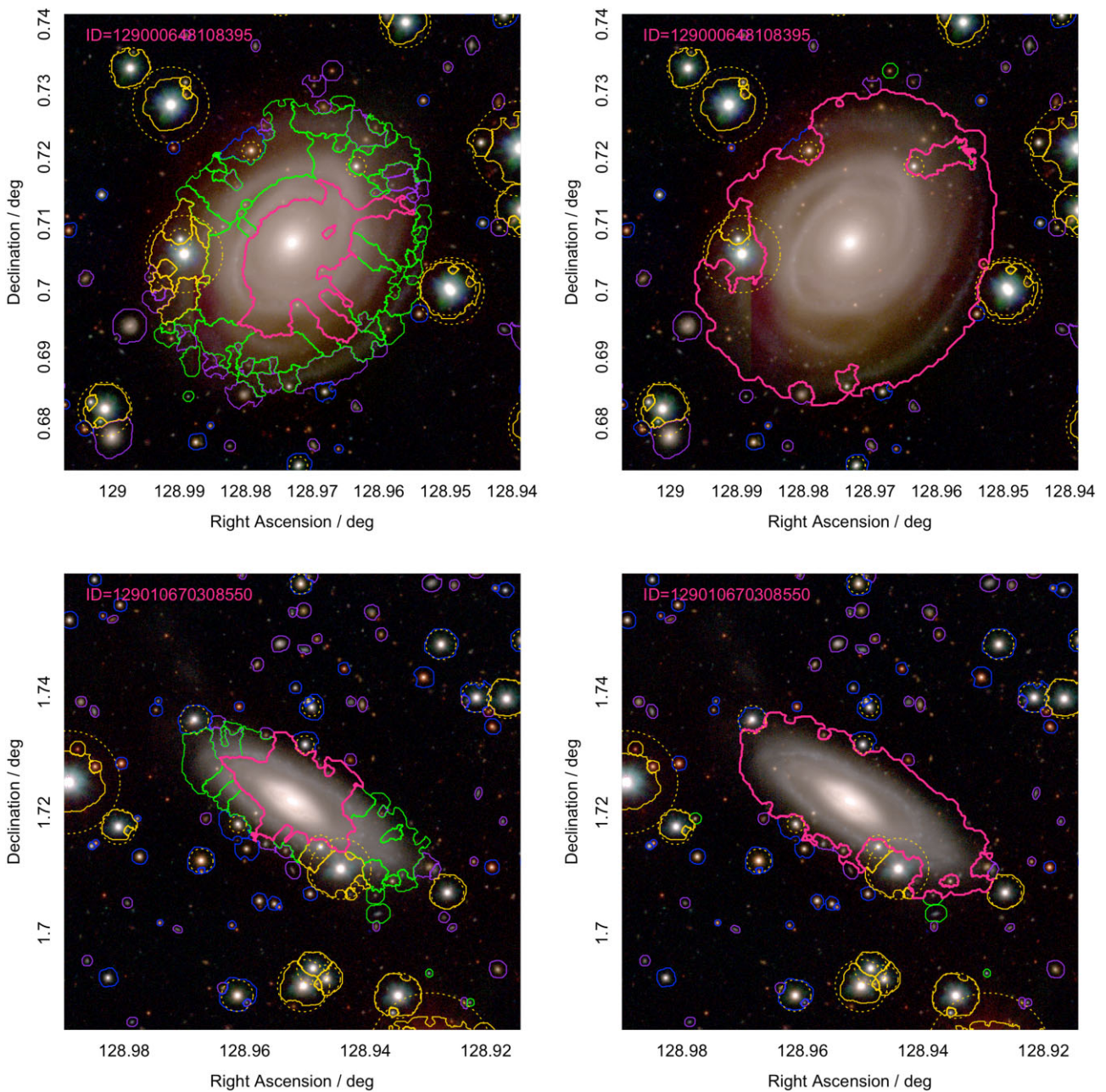
Figure 3. (Left-hand side) Two examples of nearby bright galaxies that required manual fixing and (right-hand side) after fixing. The images show *grZ* colour composites with the main object shown with a magenta segment outline, ambiguous objects in green, unmasked stars in blue, masked objects in yellow, and galaxies as mauve. The dotted yellow circles show the extend of the starmasks.

includes some duplicates with GAMA MS. These deeper redshifts are potentially useful to constrain photo-*z* efforts which extend to fainter fluxes than the GAMA MS, and hence we include them in DR4 as G15DEEPSPECCATV01. We show their location and radial distribution on Fig. 2 as the green data points. Further efforts may be made to increase the completeness in this region to complement the DEVILS survey, and further assist in the definition of photometric redshift calibration. Users interested in obtaining access or contributing to this effort should contact the GAMA Exec.[1]

3.3 Scaled-flux matched photometric redshifts for main survey sample

With the redefinition of the GAMA main sample to KiDS+VIKING $r < 19.65$ mag selection, a number of new galaxies are introduced for which redshifts were not sought. In total, there are now 10 107 galaxies without spectroscopic redshifts (z_{spec}) within our revised magnitude limit. In order to provide an estimate of their likely redshift, we employ the empirical method of Scaled Flux Matching (SFM) recently described by Baldry et al. (2021) to derive photometric redshifts (z_{phot}). In this method, we compare the $u/g/r/i/Z/Y/J/H/K_S/W1/W2$ fluxes of each galaxy with all other galaxies, for which redshift NQ > 2 and the PROSPECT fit likelihood is
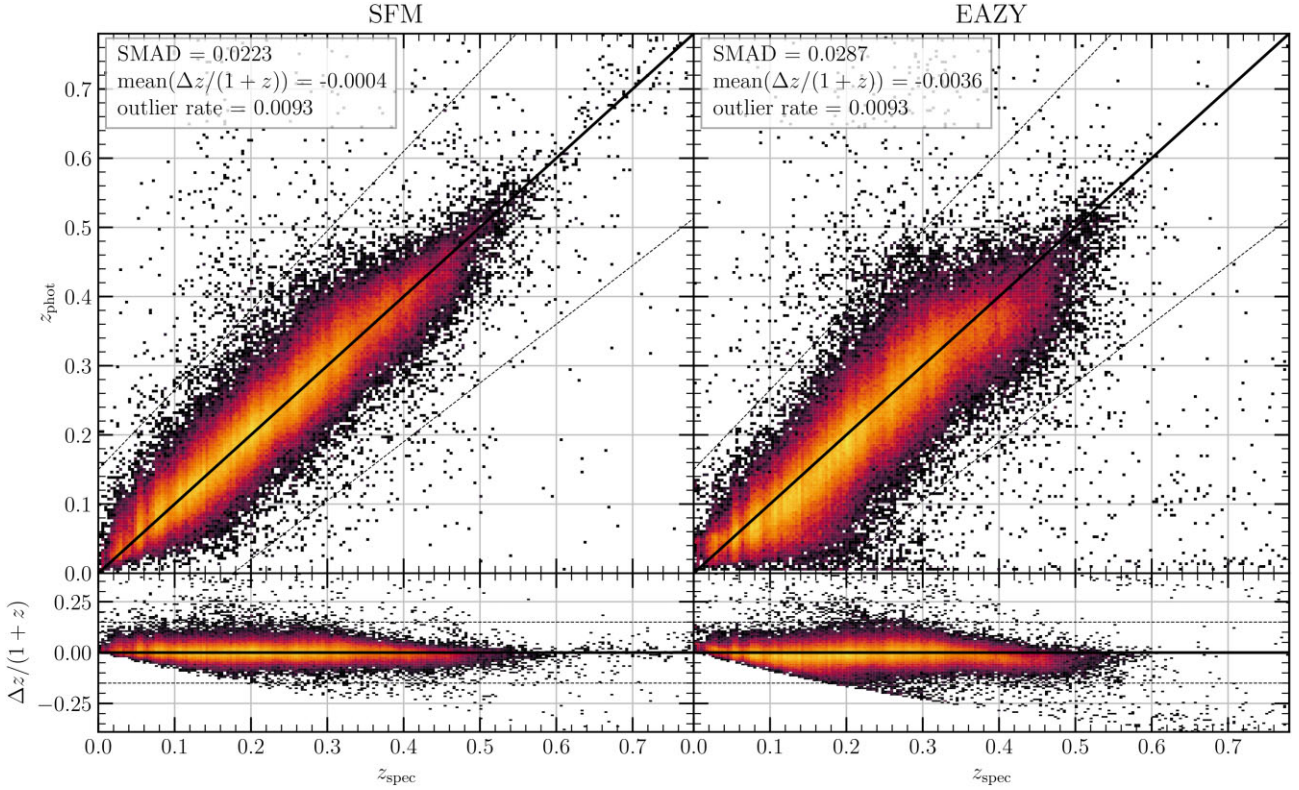
Figure 4. Comparison of spectroscopic and photometric redshifts for the GAMA sample using the SFM method on the left-hand side, and the EAZY template-matching method on the right-hand side.

> -60,[2] and determine match probabilities (with free normalization allowed). This matched sample consists of 222 991 galaxies. Relative band errors are applied in each of the bands in quadrature, consistent with the floor values used in the PROSPECT analysis by Bellstedt et al. (2020a). We, thus, produce a redshift probability distribution function (PDF) for each object as the smoothed density kernel of all scaled templates, weighted by the data-model likelihood. This allows us to derive the maximum-probability, and also the marginalized redshift value for each object. These values are indicated by the zmax and zexp columns, respectively, in the relevant DMU. An uncertainty estimate is made by determining half the 16–84th percentile range of the PDF, which is provided as zerr.

The accuracy of these photometric redshifts is demonstrated in Fig. 4 for the overall sample in terms of the Scaled Median Absolute Deviation (SMAD) given by $\text{SMAD}(x) = 1.4826 \times \text{median}(|x - \text{median}(x)|)$, and the mean offset, i.e. $\text{mean}[(1 + z)^{-1}\Delta z]$. The overall values of the SMAD and $\text{mean}[(1 + z)^{-1}\Delta z]$ are 0.0223 and -0.0004, respectively, which represents a significant improvement over more readily used, template-based methods such as EAZY (Easy and Accurate Zphot from Yale; Brammer, van Dokkum & Coppi 2008, see the discussion in Section 3.4). We note, however, that the accuracy of these redshifts is surpassed by those recently presented for the KiDS-bright sample (Bilicki et al. 2021) using ANNz, where SMAD and $\text{mean}[(1 + z)^{-1}\Delta z]$ values of 0.0180 and 0.00012, respectively, were achieved.

In Fig. 5, we show how the SMAD and $\text{mean}[(1 + z)^{-1}\Delta z]$ vary across the sample as a function of both redshift and stellar mass. The

[2]This likelihood cut eliminates galaxies with very noisy SEDs from the comparison sample.

SMAD values tend to be similar over the redshift range, displaying a slight trend towards higher values at lower stellar masses within each epoch. This highlights that the photo-z values are more precise for high-mass objects. The $\text{mean}[(1 + z)^{-1}\Delta z]$ displays more systematic variation across the sample. While the values are overall small (as is evident by the overall dark colour of the right-hand panel of Fig. 5), it is notable that out to $z \sim 0.4$, the z_{phot} values are biased slightly high for galaxies around the median stellar mass, and beyond $z \sim 0.1$, low-mass galaxies tend to have their z_{phot} values underestimated. Such trends are not apparent when assessing the bias of the sample overall. The z_{photo} values for all galaxies in the $r < 19.65$ mag sample are provided in this release as GKVSFMPHOTOZV01. For the sample of 10 107 galaxies without spectroscopic redshifts, the z_{photo} values and the PROSPECT-derived stellar masses, SFRs and gas-phase metallicities (derived in the same manner as described by Bellstedt et al. 2020a) are released as GKVSFMPHOTOZPROSPECTV01.

3.4 EAZY photometric redshifts for all sources

Template-fit photometric redshift estimates have been derived for every SED in the GKVINPUTCATV02 DMU using EAZY (Brammer et al. 2008), in combination with the Brown et al. (2014) atlas of 129 nearby galaxy spectra.

The main rationale for the choice of templates is as a complement to heavy training; the main value of these estimates lies in the use of the best available empirical templates without prejudice. Overall, we do find that the Brown et al. templates yield slightly better photoz-specz agreement in the $r_{\text{KiDSDR4}} < 19.8$ mag regime than the default EAZY template set. Hence, a potential concern is that the fixed template set is not quite flexible enough to fully map the SED-z
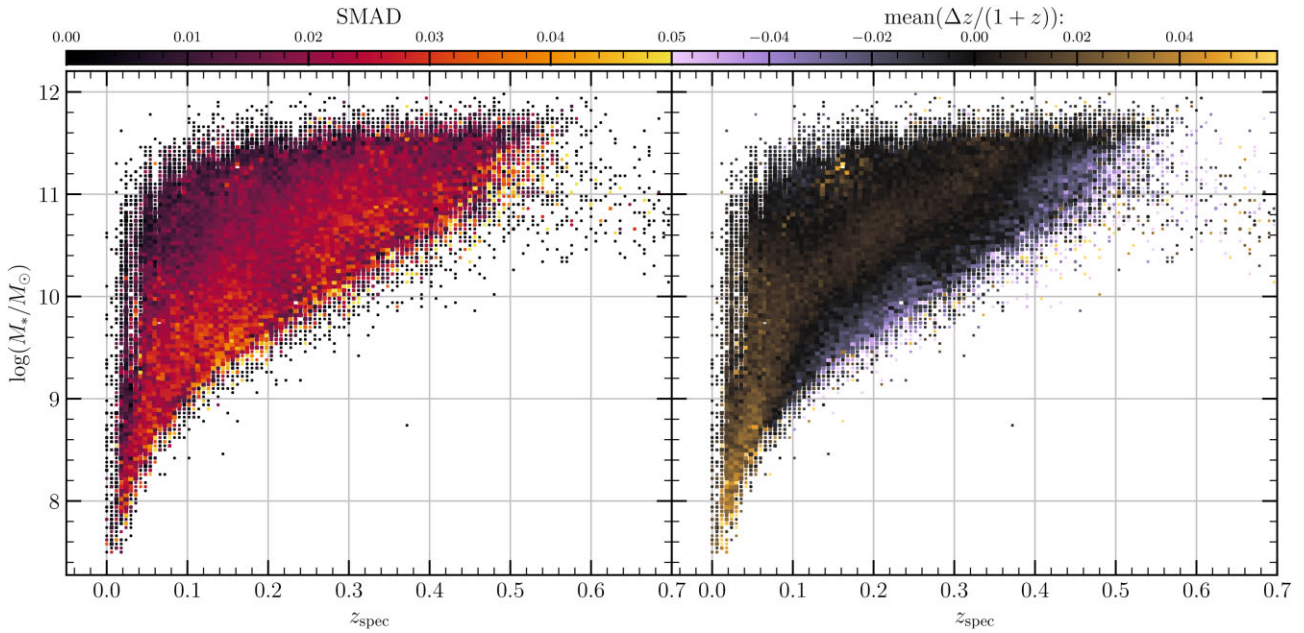
Figure 5. Demonstration of the photometric redshift accuracy for the SFM photo-*z* sample, as compared with the GAMA spectroscopic redshifts showing the variance (left-hand panel) and bias (right-hand panel) as a function of stellar mass and spectroscopic redshift. Note that the minimal colour variation in the right-hand panel is an indication that there is very little bias of the photometric redshifts across the GAMA sample.

space. We therefore experimented with two-template combinations within EAZY, and find only very minor variations in the output photo-zs, suggesting that this is not a leading source of error. The implicit assumption in using a static empirical template set is that it covers a sufficiently wide range to contain an adequate description of the optical SED for any given target: i.e. not that galaxies do not evolve, but that a low-z analogue can be found for any high-z SED. This will clearly not be true for rare and/or extreme populations (e.g. extremely metal-poor or sub-mm galaxies, etc.) or for classes that are not represented in the template set (e.g. quasars), but again the primary motivation here is to have a broadly applicable benchmark to complement more sophisticated future approaches.

These photometric redshift values are shown in Fig. 4 (right-hand side), where they are compared to the GAMA main survey spectroscopic redshifts. As for the SFM analysis the SMAD and mean$[(1 + z)^{-1}\Delta z]$ are derived, and found to be 0.0287 and -0.0036, respectively, and with a comparably small outlier rate.

These template fit photometric redshifts are intended as a valuable complement to those from machine learning and/or training sets, in several distinct but interrelated ways. First, these template-fit results are grounded in astrophysics, in the sense that they are based on actual integrated spectra from real galaxies. Secondly, because the process involves forward modelling the template spectra over many trial redshifts, it is straightforward to derive the full posterior PDF, $P(z)$. Thirdly, unlike trained approaches, they can in principle be extrapolated beyond the limit of any representative spectroscopic training/reference set. In these ways, template fit photometric redshift estimates can be extremely useful as a sanity check for, and especially in probing potential systematic biases in, results derived in other ways.

For the purposes of SED-fitting, only the *u*–*K* bands are used; the inclusion of the *GALEX* UV and *WISE* IR bands does not improve the z_{phot}–z_{spec} agreement. We also do not make use of EAZY's facility for template combination, having trialled two-template combination and found no significant improvement. We adopt the default `eazy_v1.0` template error function (Brammer et al. 2008), with amplitude 0.5, and a 0.02 mag 'systematic' uncertainty in the photometry to

soften template mismatch effects. The redshift grid spans the range 0.004–4.3 in 209 steps, with grid steps proportional to $\log(1 + z)$. We also include an original *r*-band luminosity prior, which comes from a descriptive model of the GAMA $N(m_z, z_{spec})$ distribution, extrapolated down to $r < 28$ mag. Note that this prior operates mostly to exclude too-low redshift solutions that would lead to implausibly high luminosities. It therefore has a relatively large impact on the z_{phot}–z_{spec} statistics, and plays less of a role for fainter galaxies.

The GKVEAZYPHOTOZ DMU packages the full EAZY outputs, including both maximum likelihood estimates and minimum variance estimates, evaluated with and without the luminosity prior. The preferred redshift estimate for any given galaxy is the `z_peak` value. This estimator is not well-documented, but is the prior-weighted, minimum variance estimate, evaluated in the vicinity of the maximum likelihood peak. Note that because this quantity is derived by marginalizing over the PDF, it will converge to some central value where there is insufficient information in the SED to properly constrain the redshift. We have also propagated the best-fitting template SED corresponding to the `z_peak` solution. This value is used to compute the Posterior Predictive P-Value (PPP), which is a Bayesian summary statistic that is similar to the frequentist reduced-χ^2, inasmuch as it provides an indication of goodness-of-fit. Assuming a particular model (in this case, the best-fitting template SED at `z_peak`), the PPP gives the chances of obtaining data that give a less good fit: thus, 0.5 indicates the ideal fit with reduced-χ^2 = 1; 0 would indicate a catastrophically bad fit; a value close to 1 would indicate overfitting. For each galaxy, a random draw from the posterior PDF is also given as `z_mc`; this is appropriate for describing the ensemble with Monte Carlo redshift error propagation.

The GKVEAZYPHOTOZ DMU comprises of the full photometric catalogue of 18+M sources, including artefacts and stars as well as galaxies, quasars, etc. Artefacts and stars can be excluded based on the photometric quality control flags, but it can also be useful to explore how the photometry is mapped to z_{phot} in these cases. No attempts have been made to account for SED/spectral types outside the Brown et al. (2014) spectral atlas; e.g. rare spectral types, broad-

line AGN, or QSOs; any photometric redshift estimates for such objects are likely to be meaningless. Further, there is the danger of some degree of contamination from such objects in any photometric-redshift-selected galaxy sample. In addition to the main photometric redshift catalogue, this DMU also includes the full posterior $P(z)$ for every photometric detection. We also provide analogues of the STELLARMASSES DMU (see Section 3.6 below) in a separate GKVEAZYPHOTOZSTELLARMASSES DMU. Values are derived using both the z_peak and z_mc values, containing stellar mass estimates, rest-frame photometry, and ancillary stellar population properties.

3.5 Morphological classification of the z < 0.08 GAMA sample

The improved resolution of KiDS data (FWHM ∼ 0.7 arcsec), over SDSS (FWHM ∼1.5 arcsec), along with the deeper surface brightness limit ($\Delta\mu \sim 2$ mag per square arcsec), allows us to review our previous morphological classifications. It also allows us to produce new and consistent morphological classifications across the four GAMA primary regions, and to our new nominal completeness limit of $r_{KiDSDR4} < 19.65$ mag (see Table 1). We adopt a redshift limit of $z < 0.08$ (at which point 1 arcsec = 1.51 h_{70}^{-1} kpc), which is matched to the redshift selection of our bulge-disc decomposition DMU (Casura et al., submitted). To perform the classifications, we create postage stamp images from grZ imaging (i.e. VST & VISTA). The image stamps are extracted at 30 h_{70}^{-1} kpc × h_{70}^{-1} 30 kpc scales, and with arcsinh scaling extending from $\mu_r = 15$ mag per square arcsec to the sky level. For galaxies that overflow the spatial range, we increase the stamp size accordingly based on its R100 value from GKVINPUTCATV02, which represents the approximate elliptical semimajor axis containing 100 per cent of the flux. Fig. 6 shows a random selection of images similar to those used for the classification process. Within these limits ($r_{KiDSDR4} < 19.65$ mag and $z < 0.08$), we have 15 330 galaxies which we classify into:

E: an early-type system with a single visual component

cBD: a two-component system with a compact high-surface brightness bulge

dBD a two-component system with a diffuse or extended bulge (or bulge complex)

D: a late-type system with a single visual component

C: a compact system too small to accurately classify

H: hard to classify due to extreme asymmetry (including merging components)

HE: hard to classify but the underlying galaxy is an early-type with a single visual component

FRAG: fragment of a galaxy

STAR: stellar-like and most likely not a galaxy

We note that the HE class specifically denotes early-types with what appear to be multiple cores, indicative of late-time major mergers, multiple galaxies within the halo (i.e. a compact group), or possible line-of-sight coincidences. In most of the discussion going forward, we combine the E and HE classes, but keep the distinction in the catalogue in case someone is interested in quickly finding multiple-cored early-types.

The classification process we follow is similar to that described in Hashemizadeh et al. (2021). First, we distribute the galaxies into classification directories based on criteria such as colour, size, and mass. We then assign a classifier to each directory who extracts objects for which the classification is wrong or uncertain. These are assigned to a temporary classification folder. The custodian of each class views the temporary classification folder for their class and either accepts or rejects the classification into their master set. The process is repeated until all objects are assigned. As in Hashemizadeh

et al. (2021), this process was found to be flawed, as ultimately one person is responsible for each class, and their exact definition of where the boundaries lie will vary. There is also no ability to assess the accuracy of the classifications. Hence, we implemented a final phase in which *all* classifications were reviewed and reassigned independently by SPD, S(abine)B, and LJD. This resulted in three fully independent sets of classifications allowing an assessment of classification accuracy.

Fig. 7 shows the resulting Venn diagrams for our three classifiers, and the full classification set and for each of the six sub-classes (having merged the E+HE classifications and removing the very few objects classified as STAR or FRAG). In general, the agreement is at the 90-per cent level throughout. From Fig. 7, we can see some consistent disparities between the classifiers with SPD having classified more Ellipticals than LJD or SB (denoted by the blue shading in Fig. 7 lower left). LJD identified more objects as Compact or Hard (orange shading), and SB perhaps has a slightly different dBD/cBD boundary definition (green shading). For the final classification, we take the majority decision, or in the rare case of a three-way disagreement, a final review and decision is made by SPD. The morphology DMU (GKVMORPHOLOGYV02) contains the starting classifications, classifications after the initial sort, the classifications of SPD, SB, and LJD and the final adopted classification.

Note that as part of this process, we have attempted to divide the double component systems into those with a compact-bulge (cBD), or diffuse-bulge (dBD). This classification into cBD and dBD is based solely on the visual appearance of the bulge-component, as either high surface-brightness and point-like (cBD), or low surface-brightness and extended (dBD). In due course comparisons to IFU data such as that drawn from the SAMI survey (Croom et al. 2021) can be made to determine the veracity of these sub-classifications.

If we combine the dBD and cBD classes into a single BD class, that one assumes the Compact classes are predominantly poorly resolved early-types, and the Hard class are predominantly morphologically disturbed late-types (as inspection suggests, see also Fig. 6), then the overall classification consistency changes to that shown in Fig. 8. This represents a surprisingly modest improvement suggesting that our division into six galaxy classes is meaningful. Note that only the spec-z sample is included in this analysis, as the photo-z sample was added later, and LJD did not classify this subset. Hence, the photo-z sample is essentially the classifications of SPD alone (and which will either agree or disagree with those of SB). Nevertheless, the overall agreement of the classification process, for the spec-z sample only, is 13 764/15 081 (91.3 per cent), or 13 974/15 081 (92.7 per cent) if classes are merged as E=E+HE+C, D=D+H, and BD=cBD+dBD.

To explore whether our classification accuracy is biased in stellar mass or redshift, Fig. 9 shows how the agreement varies with these two parameters. The scale is set so that 87.5-per cent agreement is coloured black and anything below varies from dark red to bright red, while higher agreement ranges from mauve to blue to green to yellow (100 per cent agreement). Here, agreement is defined for each galaxy as 0.0 if all classifiers disagree, 0.5 if two classifiers agree, and 1 if all three classifiers agree. The final value, for each bin, is then the mean of these agreement values. The size of the symbol for each bin denotes the number of objects in that bin on a logarithmic scale. Agreement across the M∗–z plane is generally consistent and above 87.5 per cent in almost all bins. There is a slight bias towards lower agreement at the lower mass high-z limit, i.e. in the direction of decreasing signal-to-noise, but still well above 87.5 per cent throughout. Hence, we conclude that our morphological classifications are robust to ≥90 per cent over the majority of the $M-z$ plane that we are sampling. Nevertheless, we note and acknowledge that morphological classification is an inexact and subjective process,
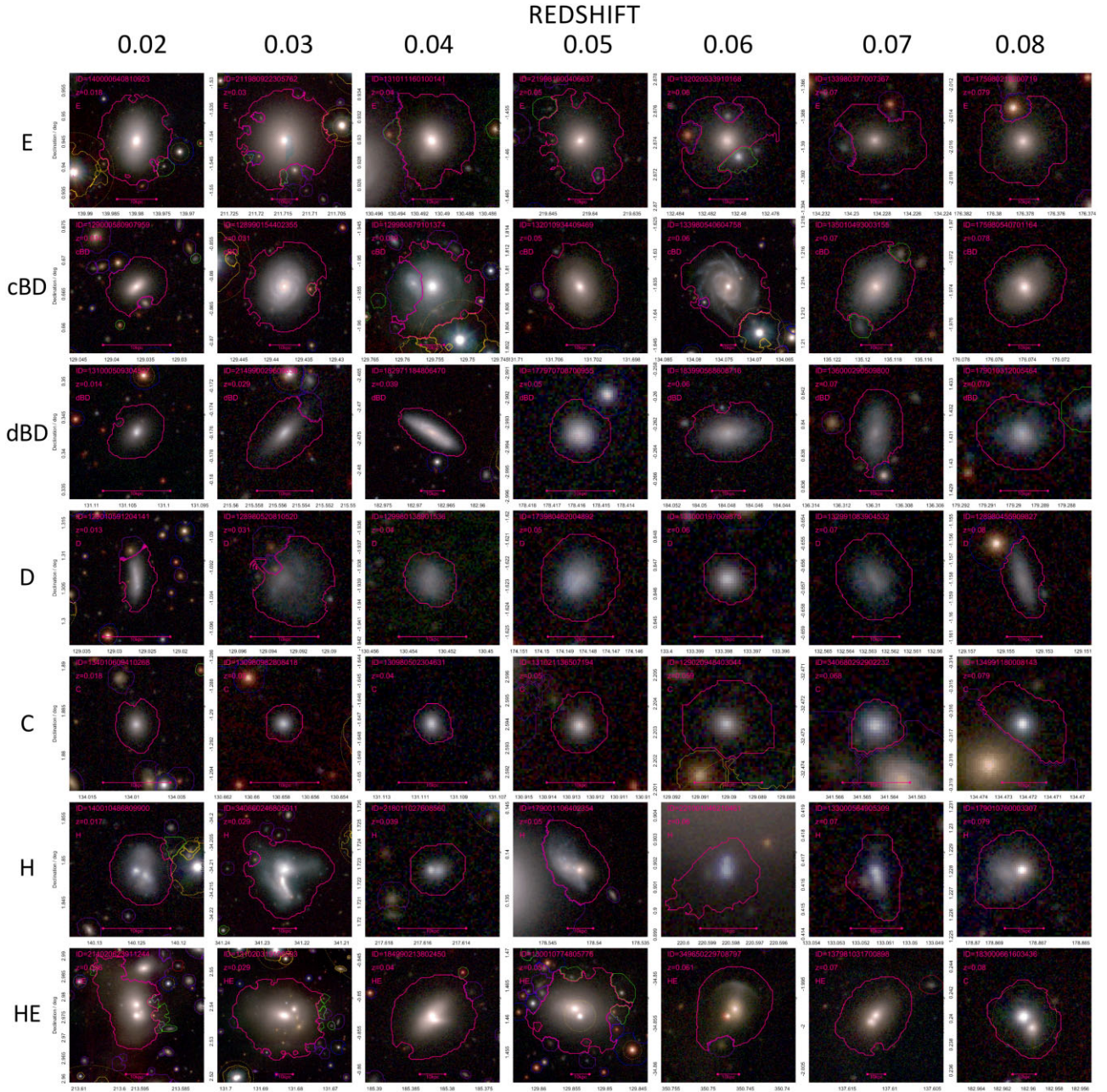
Figure 6. A sample of galaxy postage-stamp images by type and redshift, similar to those used for the morphological classification process. All stamps are displayed in *grZ* wavebands, at a resolution of $30h_{70}^{-1}$ kpc $\times 30h_{70}^{-1}$ kpc or larger (as indicated) if the image was likely to extend outside the box. The dynamical range extends from 15 mag/sq arcsec to negative median of the stamp pixel values. This selection was chosen to highlight both high and low level features using an arcsinh scaling. The magenta outline shows the segment defining the object from the Bellstedt et al. PROFOUND catalogue. Other coloured lines indicate segments for GAIA stars (yellow), faint stars (blue), GAMA galaxies (mauve), and artefacts (green).

but useful in informing whether the currently available data quality demands a two- or one-component decomposition.

3.6 Stellar mass estimates and stellar populations

Since DR3, the code for stellar mass estimation that was first described in Taylor et al. (2011) has been completely refactored. Compared to Taylor et al. (2011), the most significant change is to weight the observed SEDs such that the stellar population synthesis (SPS) modelling is done using an approximately fixed wavelength range of 3000–11 000 Å. The modelling assumes Bruzual & Charlot

(2003) stellar evolution models, assuming a Chabrier (2003) stellar initial mass function (IMF) and the Calzetti et al. (2000) dust curve. The SPS models used in the fitting are defined via a static grid in four parameters (see section 3.1 of Taylor et al. 2011); namely: time since formation (i.e. age; $8 \leq \log t_{\mathrm{form}} \leq 10.1$); *e*-folding time for the (exponentially declining) star formation history ($7.5 \leq \log \tau < 10$); stellar metallicity ($-4 \leq \log Z \leq -1.3$); and dust attenuation ($0 \leq A_V \leq 2.43$).

The values of all derived parameters given in the DMU, including the formal uncertainties, have been derived in a Bayesian way (sections 3.2–3.4 of Taylor et al. 2011), with flat priors in t_{form}, $\log \tau$,
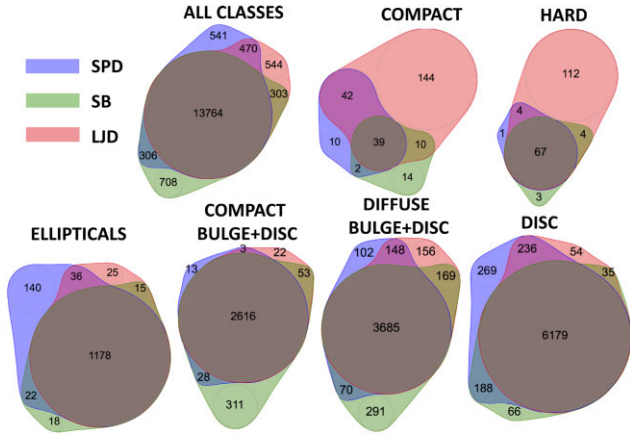
Figure 7. Venn diagrams showing the consistency and biases of the three classifiers, as indicated for the total sample (top left), or sub-classes as labelled (note that the Elliptical includes both the E and HE classes).
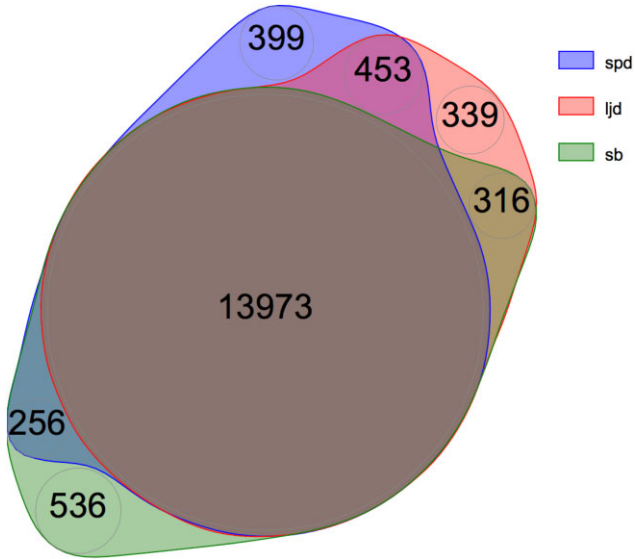

Figure 8. A Venn diagram showing the consistency of the classifications when combining the E+C+HE, D+H, and dBD+cBD classes.

log Z, and A_V. For DR4, the STELLARMASSES DMU has been updated to include stellar mass and stellar population parameters based on all the major photometric catalogues included within the GAMA data base, including: Source Extractor photometry from the Panchromatic Data Release (PDR Driver et al. 2016), matched aperture photometry from LAMBDAR (Wright et al. 2016), and the latest ProFound photometry (Bellstedt et al. 2020a) used in this paper, as well as using SDSS- or CFHT-derived photometry in the G02 field.

The differences between these simple estimates and the more sophisticated ones from ProSpect are small: random scatter of 0.13 dex; systematic offset (ProSpect masses being heavier) of 0.06 dex (see fig. 34 in Robotham et al. 2020, and associated discussions). Compared to ProSpect, the principal virtue of these stellar mass estimates is their simplicity. Using only optical-NIR photometry and simple star formation histories make it straightforward for other surveys and teams to derive directly comparable results. In other words, they provide a practical basis for robust cross-survey comparisons. For example, Taylor et al. (2011) has shown very good agreement (random scatter of 0.07 dex; systematic offest of 0.01 dex) between our *M/L*s and those used by SDSS.
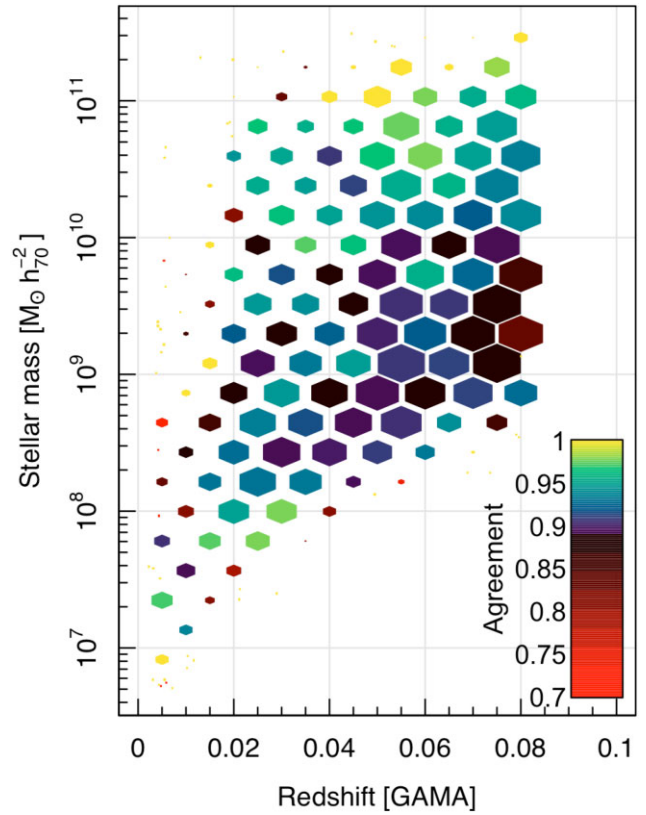
Figure 9. The morphological accuracy as a function of redshift and stellar mass. The colour of the symbol indicates the degree of agreement (see colour scale) and the size of the symbol represents the number of objects in that cell. In general, all bins are yellow, green, blue or black indicating better than 87.5 per cent agreement across the full parameter range.

3.7 Velocity dispersions

With DR4, we fill a long-standing gap in the GAMA data set with the inclusion of central stellar velocity dispersions as measured from 1D spectra. As a reflection of the depth of a galaxy's central potential well, modulo structure, velocity dispersion is a valuable complement to stellar mass estimates, and as a tracer of galaxy formation/stellar assembly history (e.g. Sheth et al. 2003; Bernardi et al. 2010; Taylor et al. 2010; Bezanson et al. 2011). The addition of velocity dispersions into the GAMA data base is particularly powerful, as they can be connected to all the many other global galaxy properties GAMA provides, including SED-derived masses, ages, SFRs, etc.; spectral absorbtion and emission diagnostics as tracers of age, metallicity, SFR, etc.; morphology, sizes, and Sérsic parameters from optical-NIR imaging; environmental metrics, group associations and masses; and more.

In brief: the velocity dispersion values are derived using pPXF (Cappellari 2017) with the MILES stellar spectral library (Sánchez-Blázquez et al. 2006; Falcón-Barroso et al. 2011) as templates. Following Bezanson et al. (2018), we use both multiplicative and additive Legendre polynomials for broad continuum subtraction of both observed and template spectra, to account for potential errors in spectral background subtraction and flux calibration. A two-pass scheme is used to identify and account for strong emission lines when fitting to the continuum: in the first pass, we complement the stellar templates with eight templates for the main emission lines; then in the second and final measurement, we retain only those lines with significant ($>5\sigma$) detections. Measurements are made and reported for all

Table 3. Data Management Units (DMUs) specifically built for the GAMA Date Release 4 (and prefixed with gkv for GAMA/KiDS/VIKING), along with version numbers, key individuals responsible for creating the DMU, and the published reference which provides the detailed description of how the DMU was produced.

DMU name	Version	Creators/contacts	Description	Reference
		GAMA/KiDS/VIKING DMUs in the DR4 data base		
GKVINPUTCAT	v02	Bellstedt, Driver, Robotham	PROFOUND photometry in FUV, NUV, *ugri*, *ZYJHK*, W1,W2 bands	Bellstedt et al. (2020a)
GKVSPECCAT	v02	Liske, Baldry	Spectroscopic redshifts	This paper
GKVSCIENCECAT	v02	Driver, Bellstedt, Robotham	Main survey selection including z's	Bellstedt et al. (2020a)
GKVFARIR	v02	Bellstedt, Robotham	PROFOUND fluxes in W3, W4, P150, P180, S250, S350, S500 bands	Bellstedt et al. (2020a)
GKVSFMPHOTOZ	v02	Bellstedt, Robotham, Baldry	Probalistic photo-z's for all $r_{KiDSDR4} < 19.65$	Baldry et al. (2021)
GKVPROSPECT	v02	Bellstedt, Robotham	PROSPECT derived info (M∗, SFR etc) for GAMA MS	Bellstedt et al. (2020b)
GKVEAZYPHOTOZ	v02	Taylor	EAZY photo-z's for *all* objects in gkvInputCatv02	This paper
GKVSTELLARMASSES	v01	Taylor	Stellar mass estimates for *all* objects in gkvInputCatv02 with reliable spectroscopic redshifts.	This paper
GKVPHOTOZSTELLARMASSES	v01	Taylor	Stellar mass estimates for EAZY and SFM photo-z's for *all* objects in gkvInputCatv02	This paper
GKVMORPHOLOGY	v02	Driver, Bellstedt, Davies	Visual morphologies to $z < 0.08$	This paper
		GAMA/KiDS/VIKING DMUs in preparation		
GKVPROFIT	v01	Casura, Liske	Profit analysis of all main survey galaxies	Casura et al, (in preparation)
GKVGROUPS	v01	Bravo, Robotham	F-o-F group catalogue for the revised GAMA main survey	Bravo et al. (in preparation)
GKVFILAMENTS	v01	Gurvarinder, Taylor, Cluver	Filament and tendril catalogue for the revised main survey	Gurvarinder et al. (in preparation)

spectra in the SpecObjAll DMU that have originated from GAMA, SDSS (Ahn et al. 2014), 2dFGRS (Colless et al. 2001), and 6dFGRS (Jones et al. 2004, 2009) and which have median continuum S/N >10 over 6383–6536 Å, as reported in the SpecLineSFRv05 DMU (Hopkins et al. 2013; Gordon et al. 2017). The main challenge to overcome has been the need to calibrate/cross-validate measurements based on the heterogenous set of spectra available. As well as direct comparison to measurements by Said et al. (2020), we have used both intra- and inter-survey comparisons to quantify/calibrate random and systematic errors in the measurements as a function of S/N, velocity dispersion, or survey (see Table 2). At a median S/N of $10 \, \text{Å}^{-1}$, typical formal errors are ∼0.06 dex for GAMA spectra, versus ∼0.03 for SDSS spectra, and ≥0.1 for both 6dFGS and 2dFGRS, and scaling approximately inversely for higher S/N. We caution that measurements from 2dFGRS spectra show greater systematic variations when compared to other data sources, presumably related to its coarser spectral resolution. A full description of the new VELOCITYDISPERSIONS DMU will be given by Dogruel et al. (in preparation).

4 GAMA DATA RELEASE 4

Tables 3 and 4 show the DMUs provided as part of GAMA Data Release 4. These are downloadable FITS tables that have been vetted via our internal quality control process and accessible via the GAMA DR4 Schema Browser, along with accompanying documentation. Any dependencies on other DMUs are clearly provided, along with the reference describing the production of the DMU (see Tables 3 and 4 Col 4). Note that, in most cases, the DMUs have been updated from the original versions (see version numbers, Tables 3 and 4 Col 2), but the methodologies remain as detailed in the papers listed in the final column of Tables 3 and 4.

4.1 Data access and good usage policy

All data are available in the form of downloadable DMUs from the GAMA DR4 website http://www.gama-survey.org/dr4 which also contains a number of basic functions allowing for DMU downloads via the Schema Browser, SQL searches, table merging, image extraction, and a single object viewer. We kindly request that researchers that make use of these data products try to adhere to the following guidelines:

(1) List the DMU name and version number of any DMU used, along with the specific column names to ensure reproduceability.

(2) Consider contacting one of the DMU authors directly, to ensure proper usage of the DMU.

(3) Include the standard GAMA acknowledgement given at http://www.gama-survey.org/pubs/ack.php

(4) Reference the key GAMA survey description papers:

(i) GAMA in general: Driver et al. (2011)

(ii) GAMA equatorial input catalogues: Baldry et al. (2010)

(iii) The GAMA spectroscopic pipeline: Hopkins et al. (2013)

(iv) The GAMA redshift measurements: Liske et al. (2015)

(v) The GAMA Data Release 4: Driver et al. (2021), i.e. this paper

(vi) Any DMU references as indicated in Tables 3 and 4

Please also note that the GAMA DR4 release is intended to be dynamic, and additional catalogues uploaded on an ongoing basis including DMUs submitted for GAMA QC by the community. If you are interested in updates, please regularly check the release website and if you are interested in submitting your own DMU to the GAMA QC process, please contact gama@eso.org or via the information on the release website.

Table 4. GAMAII DMUs included in the GAMA Date Release 4, along with version numbers, key individuals responsible for creating the DMU, and the published reference which provides the detailed description of how the DMU was produced.

DMU name	Version	Creators/contacts	Description	Reference
			GAMAII DMUs in the DR4 data base	
EQINPUTCAT	v46	Baldry	Input catalogues for the spectroscopy of the equatorial regions	Baldry et al. (2010)
G02INPUTCAT	v07	Baldry	Input catalogues for the spectroscopy of the G02 region	Baldry et al. (2018)
G23INPUTCAT	v11	Moffett, Driver	Input catalogues for the spectroscopy of the G23 region	Liske et al. (2015)
SPECCAT	v27	Liske, Baldry	All redshifts in or near the GAMA regions	Liske et al. (2015)
SPECLINESFR	v05	Owers	Line flux and equivalent width measurements for selected GAMA II spectra	Gordon et al. (2017)
LOCALFLOWCORRECTION	v14	Baldry	Redshifts from SpecCat translated into various frames	Baldry et al. (2012)
KCORRECTIONS	v05	Loveday	k-corrections in FUV, NUV, *ugriz*, *ZYJHK_s* bands for all galaxies in the equatorial regions	Loveday et al. (2012)
FILAMENTFINDING	v02	Alpaslan, Robotham	Filament and tendril catalogues	Alpaslan et al. (2014)
GALEXPHOTOMETRY	v02	Seibert, Tuffs	*GALEX* NUV and FUV photometry for the GAMA II equatorial regions	–
GEOMETRICENVIRONMENTS	v01	Eardley, Peacock	Identification of the LSS within the GAMA equatorial regions in which each point is classified as a void, sheet, filament, or knot	Eardley et al. (2015)
GROUPFINDING	v10	Robotham	GAMA Galaxy Group Catalogue (G3C) for the GAMA II equatorial and G02 fields	Robotham et al. (2011)
WISEPHOTOMETRY	v02	Cluver, Jarrett	*WISE* IR photometry for the GAMA equatorial regions	Cluver et al. (2014, 2020)
HATLASPHOTOMETRY	v03	Bourne, Liske, Driver	*Herschel* FIR photometry for *Herschel*-detected GAMA objects	Bourne et al. (2016)
LAMBDAPHOTOMETRY	v01	Wright, Robotham, Driver	21 band photometry for the GAMA equatorial regions	Wright et al. (2016)
PANCHROMATICPHOTOM	v03	Driver	Combination of various photometry catalogues from *GALEX*, SDSS, VISTA VIKING, *WISE,* and *Herschel*-ATLAS	Driver et al. (2016)
MAGPHYS	v06	Driver	MAGPHYS analysis of GAMA galaxies using LAMBDAPhotometryv03	Driver et al. (2018)
RANDOMS	v02	Farrow, Norberg	Randomly distributed galaxies with the same selection function as the main spectroscopic survey	Farrow et al. (2015)
SERSICPHOTOMETRY	v09	Kelvin, Driver, Robotham	Serisc fits in *u–K* bands using GALFIT	Kelvin et al. (2012)
STELLARMASSES	v24	Taylor	Stellar mass measurements for objects with spec-*z* in SpecObjv27	Taylor et al. (2011)
ENVIRONMENTMEASURES	v05	Brough	Environmental metrics of the local environment by density and number	Brough et al. (2013)
VISUALMORPHOLOGY	v03	Driver, Baldry	Visual morphologies based on SDSS images to $z < 0.06$	Kelvin et al. (2014)
G15DEEPSPECCATV01	v01	Davies, Driver	Redshifts obtained in a 1 deg^2 sub-region within the GAMA 15-h region	This paper
VELOCITYDISPERSIONS	v01	Taylor	Velocity dispersion measurements for all objects in SpecObjv27	Dogruel et al. (in preparation)

5 THE GALAXY STELLAR MASS FUNCTION AT $z < 0.1$

We conclude this release by providing a revised estimate of the low-*z* GSMF, and its sub-division by morphological type. This builds on earlier GAMA works on these topics from Baldry et al. (2012), Kelvin et al. (2014), Moffett et al. (2016), and Wright et al. (2017). Specifically, our revised estimate will make use of the following DMUs: SPECCATV27 for the redshifts, GKVSCIENCECATV02 for the photometric measurements, GKVMORPHOLOGYV02 for Hubble Classifications, GKVPROSPECTV02 for the Stellar Masses measurements and uncertainties, and GKVSFMPHOTOZV02 for photometric redshifts and stellar masses of Main Survey objects without spectroscopic redshifts. These DMUs are all included in DR4, see Tables 3 and

4, and are available from the release website. The key advances over our previous GSMF estimates are the inclusion of the G23 region, the upgrade to KiDS photometry, revised stellar masses, and the inclusion of photometric data for missing and/or low surface brightness systems.

We note that in this work, we do not attempt to identify and remove AGN. In two forthcoming papers, Thorne et al. (submitted and in preparation), we explore the AGN contribution and its impact on our PROSPECT stellar mass estimates in detail.

We now start by adopting the magnitude limit of $r_{KiDSDR4} = 19.65$ mag, as discussed in Section 2.2, for the four primary GAMA regions (G09, G12, G15, and G23). This sub-sample contains 205 540 galaxies for which our survey is 95.1 per cent complete in terms of reliable spectroscopic redshifts (see Section 2.2). For those galaxies
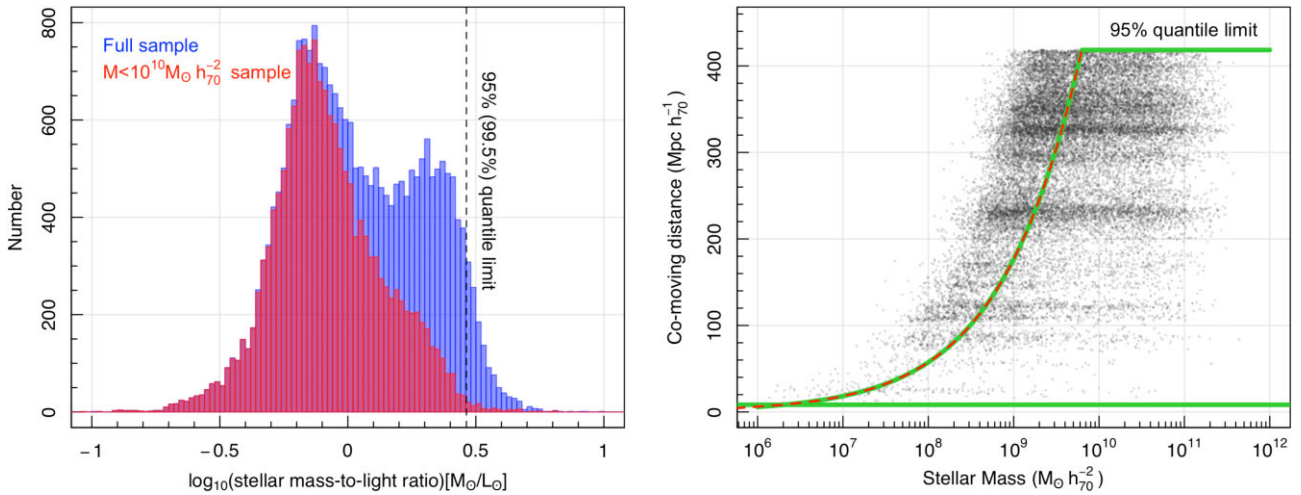
Figure 10. (Left-hand panel) Shows the mass-to-light ratio of the galaxies in our sample (blue histogram) along with the dashed line which delineates the 95-percentile value and the lower mass population impacted by this cut (red histogram) and for which our selection encloses 99.45 per cent of the sample. (Right-hand panel) Shows the total sample in the stellar mass distance plane. The red dashed line shows the implied mass completeness limit from a combination of the given flux limit of $r = 19.65$ mag combined with the 95 percentile mass-to-light limit derived from the left-hand panel. The green line shows the final selection function.

without spectroscopic redshifts, we adopt the photometric redshift from GKVSFMPHOTOZV02, as described in Section 2.3. Hence, we deem our sample to be 100 per cent redshift complete. We now limit our sample to the nearby Universe by imposing a redshift cutoff of $z < 0.1$. Note that no attempt is made to fold in any evolution within the interval $0 < z < 0.1$ (but see later discussion in Section 6.2).

To reduce the observed sample to an empirical mass function, we make use of Modified Maximum Likelihood (MML) estimation, as developed by Obreschkow et al. (2018). This method avoids binning the data, and is a Bayesian framework for fitting distribution functions to complex multidimensional data, developed particularly for galaxy mass functions. By design, the MML framework includes due consideration of the observational measurement errors for each individual object, optimal correction for systemic Eddington bias, the ability to incorporate complex observational selection functions, and the option to correct internally for the underlying large-scale structure (LSS) identified within the survey volume. At its heart, the MML approach consists of an iterative fitting algorithm that successively solves a standard maximum likelihood estimation and then updates the data by accounting for the previous fit and the observational uncertainties. The power of this 'fit-and-debias' procedure relies on the fact that its solution can be shown to converge towards the exact solution of a much more expensive full Bayesian hierarchical model, in which each observable (e.g. each galaxy mass) is a free parameter with a prior given by the measurement (e.g. flux and redshift).

The MML framework is accessible via DFTOOLS (Obreschkow et al. 2018), an open-source software package for the R statistical programming language. The code is fully documented and many examples have been provided by Obreschkow et al. (2018). DFTOOLS can be used to derive volume-corrected binned mass functions, as well as to fit parametrized analytical functions. In both cases, DFTOOLS can determine the most likely solutions and full co-variance matrices of the relevant model parameters. Here, we elect to fit a double Schechter function, able to tackle the characteristic upturn seen at intermediate stellar mass by Baldry et al. (2012) and in subsequent studies. This function is defined in Baldry et al. (2012)

as

$$\phi_M \mathrm{d}M = \mathrm{e}^{-M/M^*} \left(\phi_1^* \left(\frac{M}{M_*} \right)^{\alpha_1} + \phi_2^* \left(\frac{M}{M_*} \right)^{\alpha_2} \right) \frac{\mathrm{d}M}{M^*}, \qquad (1)$$

where $\phi_M \mathrm{d}M$ is the number density of galaxies in the mass interval dM and ϕ_1^*, ϕ_2^* and α_1, α_2 describe the normalization and slope parameters, respectively, for the two components. Without loss of generality, we can always choose $\alpha_1 > \alpha_2$ such that the second term in equation 1 dominates at lower masses.

In our usage of DFTOOLS, we adopt the stellar mass errors identified for each galaxy from the PROSPECT analysis of Bellstedt et al. (2020b). The median error for our $z < 0.1$ sample is $\Delta \log_{10} M = 0.043$. In those cases, where photometric redshifts are used, the errors also include the uncertainty in the redshift (see Section 2.3), although we note that in our final analysis, only 98 galaxies with photometric redshifts, (i.e. 0.7 per cent) survive through to the final sample.

The observational selection function is the key component to deriving the appropriate volume correction. Given the data are flux limited in the observed r-band, yet we are looking to recover stellar mass functions, this is non-trivial. To overcome this issue, we explore the r-band mass-to-light distribution as shown in the left-hand panel of Fig. 10. The blue distribution shows the spread and the dashed line shows the mass-to-light ratio that encloses 95 per cent of the full distribution, i.e. $\log_{10}(M/L_r) = 0.463$. Note that if we only consider galaxies with stellar masses below 10^{10} M$_\odot$ h_{70}^{-2} (i.e. those not seen over the entire volume), we find only 0.55 per cent with mass-to-light ratios above 0.463 (see the red shaded histogram in Fig. 10). Hence, in effect, our cut is valid for 99.45 per cent of the population impacted by the selection boundary. Fig. 10 (right-hand panel) now shows our full sample in terms of their stellar mass and co-moving distance as grey dots, and where the LSS (horizontal banding) is clearly visible. Using our r_{KiDSDR4}-band limit of 19.65 mag, combined with our 95 per cent mass-to-light limit (dashed line of Fig. 10 left-hand panel), we can now define the red dashed line. This denotes the distance limit at each redshift for which our sample will be 99.5 per cent complete for $M < 10^{10}$ M$_\odot$ h_{70}^{-2}. We fit the dashed red curve on Fig. 10 (right-hand panel) with a generalized logistics function, also

Table 5. Key values defining the Richards curve selection function parameters for various samples (as indicated).

Galaxy sample	Redshift z	Number of galaxies remaining (starting)	$\log_{10}\left[\frac{M}{L_r}\right]_{95\text{per cent limit}}$ $(M_\odot/L_\odot)$	A	K	C	B	M	ν
Total	$z < 0.10$	13 957 (24 082)	0.463	−0.0160	2742.0	0.9412	1.1483	11.815	1.691
E+HE	$z < 0.08$	1272 (1355)	0.506	−0.1232	2512.6	0.1411	1.1460	10.233	0.285
cBD	$z < 0.08$	2638 (2713)	0.497	−0.0605	2517.7	0.4758	1.1469	11.274	0.948
dBD	$z < 0.08$	2799 (4138)	0.405	−0.0124	2521.6	1.5262	1.1465	12.205	3.042
D	$z < 0.08$	3116 (6896)	0.299	−0.0146	2157.0	0.5619	1.1477	11.212	1.296
C	$z < 0.08$	38 (112)	0.396	−0.1197	2399.7	0.0933	1.1460	9.761	0.197
H	$z < 0.08$	40 (79)	0.443	−0.1064	3138.3	0.4670	1.1462	11.212	0.753

known as a Richards curve, defined as follows

$$y(x) = A + \frac{K - A}{(C + e^{-B(x-M)})^{1/\nu}}. \tag{2}$$

Here, y represents the co-moving distance limit, and x the mass-limit, while the fitted parameters: A, K, C, B, M, and ν define the upper and lower asymptotes and the shape of the transition curve. Table 5 shows the fitted Richards curve parameters determined for the full sample (All), or independently for each morphological class. The fit is shown as the green curve on Fig. 10 (right-hand panel) and follows the red dashed line extremely closely. Finally, we truncate the green line at our minimum redshift ($z > 0.0013$) to avoid stellar contamination, and our maximum redshift ($z < 0.1$), to define our final sample selection boundary. Although, we have essentially rejected 50 per cent of our original $z < 0.1$ sample, we have now transformed the sample from an r-band selected one to a near (99.5 per cent) mass-limited one with a very precisely defined selection function.

The sample is now restricted to those galaxies that lie within the limits defined by our selection function. We input the selected galaxies' co-moving distances, stellar masses, stellar mass errors, selection function, and desired functional form to fit into the DFTOOLS routine DFFIT. This code returns the binned co-moving space density distribution (see Table 6), the functional fit (see Table 7), and the full co-variance matrix for the fitted parameters. Fig. 11 shows the combined GSMF data (black circles with yellow fill), along with the results for each of the four GAMA regions separately (coloured discs).

Given a survey selection function and a specific model for the MF (e.g. a parametric Schechter function or a binned step-wise MF), the most likely cosmic density *variations* as a function of mass caused by cosmic LSS can be determined simultaneously while fitting the free parameters of the MF model. Intuitively speaking, this is possible, because a smooth selection function and a smooth MF normally predict a smooth source count as a function of mass. A comparison to the actual source count, then allows us to infer the LSS-driven fluctuations. The mathematics and explicit form of the likelihood function can be found in Obreschkow et al. (2018, section 2.3). The only unknown in this automatic LSS correction is the *overall* density normalization of the survey volume. This we fix manually by imposing the condition that the total mass within the whole survey volume is unbiased.

In the left-hand panel, the DFTOOLS inbuilt LSS correction is not implemented, and in the right-hand panel it is bringing the fields into good alignment. In general the four regions agree well, showing a variation consistent with what one might expect from cosmic variance considerations of 25 per cent per GAMA region. We note that the binned data for the total distribution (black circles with yellow fill) appear to exhibit a smooth distribution and extent, with reasonable statistics, over the stellar mass range from $10^{6.75}\,M_\odot\,h_{70}^{-2}$ to $10^{11.5}\,M_\odot\,h_{70}^{-2}$.

Comparing the GSMF derived for the four individual fields without the LSS correction (i.e. Fig. 11 left-hand panel), we see that the G23 region has both the highest mass density as well as the steepest low mass upturn. This steep upturn is reminiscent of the mass function seen in the Virgo cluster. There is therefore some possibility that the G23 region may intersect with an as yet undefined very nearby loosely bound group. This is not explored here, but will be considered as we obtain 21-cm radio observations in this region. We also note that G12 exhibits a slightly steeper low-mass end, and lies a few degrees offset from the Virgo Southern spur (see Ferrarese et al. 2012 their fig. 1). With the LSS correction implemented (i.e. Fig. 11 right-hand panel), we see the four fields brought into closer alignment. It is reassuring that both with and without the LSS correction, the overall GSMF is identical suggesting that the combination of the four distinct fields goes a long way towards ironing out the LSS.

Finally, we note that both with and without the LSS correction, the G09 region (red data points) appears underdense, this has been a feature noted and highlighted in earlier GAMA papers and arguably sets the G09 field slightly apart. In Section 6, we will explore GAMA's overall over/under density relative to a 5012 deg² SDSS selected region. In due course, two imminent surveys will improve upon our measurements, namely the Wide Area VISTA Extragalactic Survey (Driver et al. 2019) which will survey 1150 deg² in two distinct regions to $m_Z \sim 21$ mag, and the recently commenced DESI Bright Galaxy Survey (Ruiz-Macias et al. 2020) which will survey 14000 deg² to a comparable depth as GAMA.

5.1 Comparison to previous measurements

Fig. 12 (upper) shows our derived GSMF (with the LSS correction implemented), for the combined GAMA sample (red dots), and compared to our earlier GAMA measurements as well as notable literature values (as indicated). Also shown is the Local Group compendium of McConnachie (2012) (updated to October 2019 via http://www.astro.uvic.ca/~alan/Nearby_Dwarf_Database.html), and the local sphere compendium of Karachentsev & Kaisina (2019). Note that many of the surveys shown, start to suffer from incompleteness at masses below $10^8\,M_\odot$, and these are indicated by lower limits (shown as arrows). In general, the plot shows reasonable consistency across the data sets with the exception of the very high mass and very low mass ends.

On Fig. 12 (centre panel), we replot the same base data but with the fitted double Schechter function now divided out and the GAMA data points shown in 0.125 dex mass bins (rather than 0.25 dex mass bins in the upper and lower panels). Note that the grey lines show a 1σ sampling of the co-variance matrix of the fit (in all three panels), to highlight the fit uncertainty. Not surprisingly, the red data points, to which the double Schechter function has been fitted, scatter around the flat line. Most of the other surveys show overlap within their

Table 6. The galaxy stellar mass number-density distributions for the full sample and for each GAMA region at $z < 0.1$. No detections in a bin are indicated by a blank entry. Note that the tabulated values *DO NOT* include the re-normalization to SDSS, or correction to redshift zero (see Section 6). To apply these corrections, add 0.0807 dex to all number-density values.

$\log_{10}(M)$ ($M_\odot\,h_{70}^{-2}$)	$\log_{10}$ number-density of galaxies per dex per $Mpc^3\,h_{70}^{-3}$				
	All	G09	G12	G15	G23
11.875	–	–	–	–	–
11.625	-4.704 ± 0.138	-4.997 ± 0.301	-5.028 ± 0.301	–	-4.204 ± 0.125
11.375	-3.414 ± 0.032	-3.492 ± 0.075	-3.356 ± 0.060	-3.507 ± 0.067	-3.310 ± 0.06
11.125	-2.922 ± 0.019	-3.010 ± 0.043	-2.878 ± 0.035	-2.985 ± 0.041	-2.818 ± 0.034
10.875	-2.561 ± 0.013	-2.652 ± 0.029	-2.504 ± 0.023	-2.561 ± 0.025	-2.517 ± 0.025
10.625	-2.361 ± 0.010	-2.440 ± 0.022	-2.299 ± 0.018	-2.371 ± 0.021	-2.324 ± 0.020
10.375	-2.292 ± 0.009	-2.389 ± 0.021	-2.244 ± 0.017	-2.284 ± 0.019	-2.242 ± 0.018
10.125	-2.274 ± 0.009	-2.352 ± 0.020	-2.202 ± 0.017	-2.277 ± 0.018	-2.256 ± 0.018
9.875	-2.219 ± 0.009	-2.314 ± 0.020	-2.148 ± 0.015	-2.232 ± 0.018	-2.178 ± 0.017
9.625	-2.142 ± 0.010	-2.263 ± 0.023	-2.074 ± 0.019	-2.117 ± 0.019	-2.109 ± 0.021
9.375	-2.055 ± 0.014	-2.158 ± 0.027	-1.940 ± 0.031	-2.101 ± 0.025	-1.976 ± 0.030
9.125	-1.886 ± 0.020	-2.044 ± 0.042	-1.794 ± 0.035	-1.866 ± 0.031	-1.871 ± 0.048
8.875	-1.795 ± 0.024	-2.018 ± 0.058	-1.710 ± 0.041	-1.771 ± 0.039	-1.744 ± 0.053
8.625	-1.688 ± 0.032	-1.739 ± 0.064	-1.613 ± 0.044	-1.575 ± 0.055	-1.655 ± 0.105
8.375	-1.669 ± 0.045	-1.717 ± 0.089	-1.711 ± 0.064	-1.834 ± 0.176	-1.667 ± 0.222
8.125	-1.544 ± 0.071	-1.697 ± 0.097	-1.552 ± 0.146	-1.453 ± 0.138	-1.537 ± 0.222
7.875	-1.287 ± 0.079	-1.351 ± 0.125	-1.490 ± 0.176	-1.331 ± 0.125	-0.943 ± 0.125
7.625	-1.349 ± 0.092	-1.413 ± 0.176	-0.956 ± 0.097	-1.786 ± 0.222	–
7.375	-1.011 ± 0.071	-0.986 ± 0.222	-0.819 ± 0.114	-1.130 ± 0.097	-1.046 ± 0.222
7.125	-1.084 ± 0.125	–	-0.806 ± 0.146	-1.741 ± 0.301	–
6.875	-0.691 ± 0.176	–	-0.564 ± 0.222	-0.833 ± 0.301	–
6.625	–	–	–	–	–
6.375	0.202 ± 0.176	–	0.173 ± 0.301	-0.098 ± 0.301	–
6.125	–	–	–	–	–

Table 7. GAMA GSMFs for various regions ($z < 0.1$). Note that the $\log_{10}(\phi*)$ values *DO NOT* include the renormalization to SDSS, or the correction to redshift zero (see Section 6). To apply these corrections, add 0.0807 dex to both $\log_{10}(\phi*)$ values.

Data set	$\log_{10}(M*)$ ($M_\odot\,h_{70}^{-2}$)	$\log_{10}(\phi_1^*)$ ($Mpc^{-3}\,h_{70}^3$)	$\log_{10}(\phi_2^*)$ ($Mpc^{-3}\,h_{70}^3$)	α_1	α_2	$\log_{10}(\rho_*)$ ($M_\odot\,Mpc^{-3}\,h_{70}$)
All	10.745 ± 0.020	-2.437 ± 0.016	-3.201 ± 0.064	-0.466 ± 0.069	-1.530 ± 0.027	8.392 ± 0.006
G09	10.764 ± 0.044	-2.513 ± 0.035	-3.462 ± 0.204	-0.577 ± 0.144	-1.583 ± 0.084	8.310 ± 0.017
G12	10.737 ± 0.037	-2.373 ± 0.029	-3.155 ± 0.114	-0.469 ± 0.126	-1.557 ± 0.045	8.453 ± 0.012
G15	10.666 ± 0.038	-2.411 ± 0.030	-3.048 ± 0.088	-0.265 ± 0.141	-1.474 ± 0.041	8.374 ± 0.012
G23	10.800 ± 0.043	-2.438 ± 0.037	-3.167 ± 0.166	-0.515 ± 0.157	-1.512 ± 0.075	8.456 ± 0.017

Note. †Cosmic (sample) variance error.

quoted errors. The one obvious discrepancy is with the SDSS data of Bernardi et al. (2018), where we see what looks like a systematic offset at the very high mass end. Bernardi et al. (2018) explore, in detail, the difficulties of estimating the very high-mass end correctly, and provide a range of possible mass estimations, highlighting that the uncertainty is due to many potential factors related to: significant photometric corrections applied to the high-mass SDSS data; the importance of the stellar population assumptions; and the role of dust. At this stage, we are not overly concerned, but note that where both GAMA and SDSS statistics are good the surveys appear to agree well within the errors, with perhaps some indication of incompleteness at the SDSS low-mass end at $\sim 10^9\,M_\odot\,h_{70}^{-2}$ (as one might expect from its shallower surface brightness limit of 23 mag per $arcsec^2$). We revisit this topic later in Section 6 following renormalization of the GAMA data to the SDSS volume.

Included in the data shown on Fig. 12 are the narrow-band photometric redshift data from the COSMOS15 release Laigle et al. (2016) as used by Wright et al. (2017) to determine a GSMF to very low stellar masses (gold triangles). The Wright et al. (2017) result used the combination of GAMA and COSMOS15 data, extending the

GSMF down to $10^7\,M_\odot\,h_{70}^{-2}$ but with the caveat of increased errors, and the potential for a systematic bias in the very low photometric redshift estimates (and reflected in the errors). Despite these caveats, the agreement is good, although see further discussion in Section 6.3. In the end, our deeper analysis suggests these corrections may have been overestimated. We extend this work by now showing the $z < 0.1$ GSMF from the DEVILS survey (Davies et al. 2018).

The DEVILS data are a combination of many contributing surveys that provide narrow-band photometric, spectroscopic, or grism data, as detailed in Thorne et al. (2021; see their Appendix C). Stellar masses for these data were determined by Thorne et al. (2021) using the same PROSPECT code as used for the GAMA data (i.e. Bellstedt et al. 2020b). In plotting the Thorne et al. data, we need to incorporate an Eddington bias correction. This is due to the combination of the photometric redshift error with the solid angle on the sky, resulting in more high-z galaxies being scattered to $z < 0.1$, than low-z galaxies scattered above. We estimate the scale of this effect by running a set of Monte Carlo simulations in which we perturb the redshift values by their quoted errors, and recompute the DEVILS GSMF after scaling the masses for the redshift change. We estimate the Eddington

Table 8. The galaxy stellar mass number-density distributions for various morphological types for $z < 0.08$. No detections in a bin are indicated by a blank entry. Note that the tabulated values *DO NOT* include the re-normalization to SDSS, or correction to redshift zero (see Section 6). To apply these corrections, add 0.0866 dex to all number-density values.

| $\log_{10}(M)$ ($M_\odot\, h_{70}^{-2}$)	E+HE	cBD	dBD	D	H	C
			Number-density of galaxies per dex per $Mpc^3\, h_{70}^{-3}$			
11.875	–	–	–	–	–	–
11.625	-4.623 ± 0.146	–	–	–	–	–
11.375	-3.483 ± 0.048	-4.146 ± 0.103	-5.021 ± 0.176	–	-5.322 ± 0.301	–
11.125	-3.164 ± 0.035	-3.383 ± 0.043	-4.281 ± 0.105	-4.845 ± 0.222	-5.021 ± 0.176	–
10.875	-3.074 ± 0.031	-2.746 ± 0.021	-3.669 ± 0.063	-4.322 ± 0.114	-4.720 ± 0.176	-5.322 ± 0.301
10.625	-2.992 ± 0.029	-2.543 ± 0.017	-3.354 ± 0.044	-3.766 ± 0.067	-4.845 ± 0.222	-5.322 ± 0.301
10.375	-3.008 ± 0.029	-2.549 ± 0.017	-3.084 ± 0.031	-3.318 ± 0.041	-4.623 ± 0.146	-5.322 ± 0.301
10.125	-3.077 ± 0.031	-2.667 ± 0.020	-2.819 ± 0.024	-3.039 ± 0.031	-4.544 ± 0.125	–
9.875	-3.202 ± 0.035	-2.909 ± 0.026	-2.576 ± 0.018	-2.824 ± 0.024	-4.544 ± 0.125	-4.845 ± 0.222
9.625	-3.323 ± 0.041	-3.166 ± 0.035	-2.502 ± 0.016	-2.537 ± 0.017	-4.528 ± 0.125	-5.021 ± 0.176
9.375	-3.491 ± 0.075	-3.138 ± 0.047	-2.453 ± 0.020	-2.401 ± 0.016	-4.110 ± 0.125	-3.978 ± 0.125
9.125	-3.334 ± 0.087	-3.125 ± 0.074	-2.372 ± 0.027	-2.222 ± 0.019	-4.021 ± 0.146	-4.736 ± 0.301
8.875	-3.157 ± 0.097	-3.081 ± 0.103	-2.278 ± 0.037	-2.129 ± 0.026	-3.965 ± 0.222	-3.425 ± 0.125
8.625	-4.022 ± 0.301	-3.015 ± 0.155	-2.183 ± 0.047	-1.878 ± 0.030	-3.695 ± 0.176	-3.366 ± 0.222
8.375	–	–	-2.186 ± 0.077	-1.837 ± 0.043	-3.475 ± 0.176	-3.613 ± 0.301
8.125	–	–	-2.367 ± 0.114	-1.919 ± 0.071	–	-3.175 ± 0.301
7.875	–	–	-2.031 ± 0.138	-1.591 ± 0.074	–	–
7.625	–	-2.386 ± 0.301	-2.471 ± 0.301	-1.348 ± 0.089	–	–
7.375	–	–	-1.629 ± 0.222	-0.838 ± 0.077	–	–
7.125	–	–	–	-0.938 ± 0.114	–	–
6.875	–	–	–	-1.098 ± 0.222	–	-1.241 ± 0.301
6.625	–	–	–	-1.080 ± 0.301	–	–
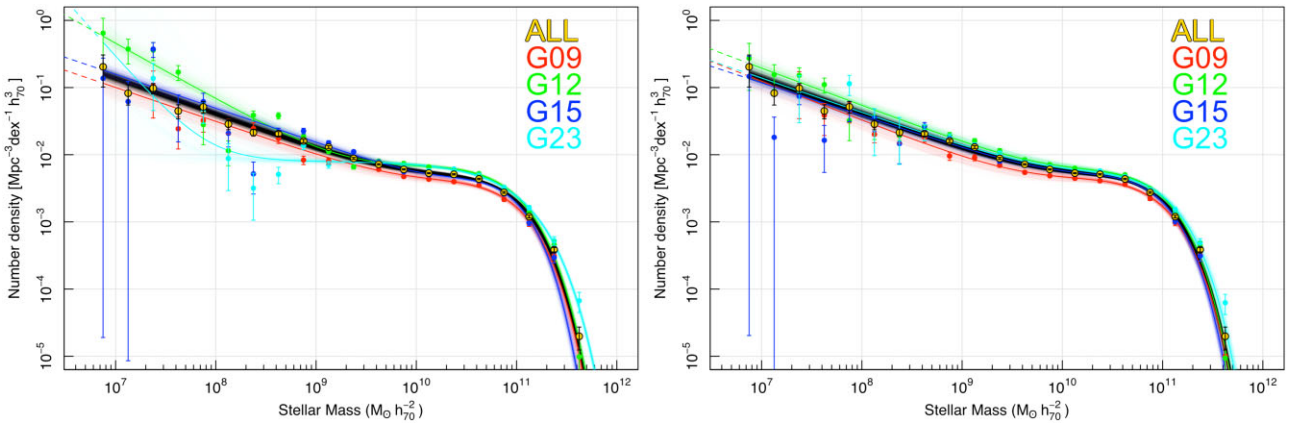
Figure 11. The recovered GSMF for the combined data (shown as the black circles with yellow infill and black lines), and for each of the four regions shown individually with the colours as indicated in the figure key. The left-hand panel shows the results without implementing the DFFIT LSS correction, and the right-hand panel with. Generally the overall GSMF is unchanged, but the GSMF for each region is brought into much greater alignment.

bias from the change in the GSMF measurements, and correct the original GSMF by this amount. In effect, we are introducing an additional Eddington bias to determine its approximate impact, and then removing this from the original distribution. The data points move *systematically* downwards but within their original errors. Following this correction, we see that the DEVILS $z < 0.1$ data (green diamonds) agree well with the GAMA $z < 0.1$ data to the GAMA mass limit.

While the errors on the DEVILS data are large, this agreement is encouraging as DEVILS imaging is based on much deeper Subaru data than the ESO KiDS data. This agreement would be unlikely to occur if DEVILS was identifying a significant additional low-z population not seen in the ESO KiDS data, e.g. due to surface brightness considerations. While these agreements are tentative – because one cannot rule out a bias in the photometric estimation that

acts to emulate a surface brightness bias in the GAMA data – the consistency between these results, Wright et al. (2017) and Thorne et al. (2021) is reassuring.

As noticed in previous papers, and in particular Baldry et al. (2012), the GSMF appears to exhibit a plateau around $10^{9.5}$ to $10^{10.5}\, M_\odot\, h_{70}^{-2}$. This feature *may* be due to a higher late-time merger rate at the high-mass end, as argued by Robotham et al. (2014). This distinctive feature has been shown to emerge at lower redshift ($z < 1$) by Wright, Driver & Robotham (2018) in their compendium of GSMF's from $z = 5$ to 0. At lower masses, the GSMF turns up at $10^{9.5}\, M_\odot\, h_{70}^{-2}$ and exhibits a linear slope [in $\log(\phi) - \log(M_*)$ space] to the completeness limit. This trend is now extended by the new data to $10^{6.75}\, M_\odot\, h_{70}^{-2}$ with no obvious sign of any significant downturn or flattening. Hence, the most numerous type of galaxy in the nearby Universe must have a mass at, or more likely below,
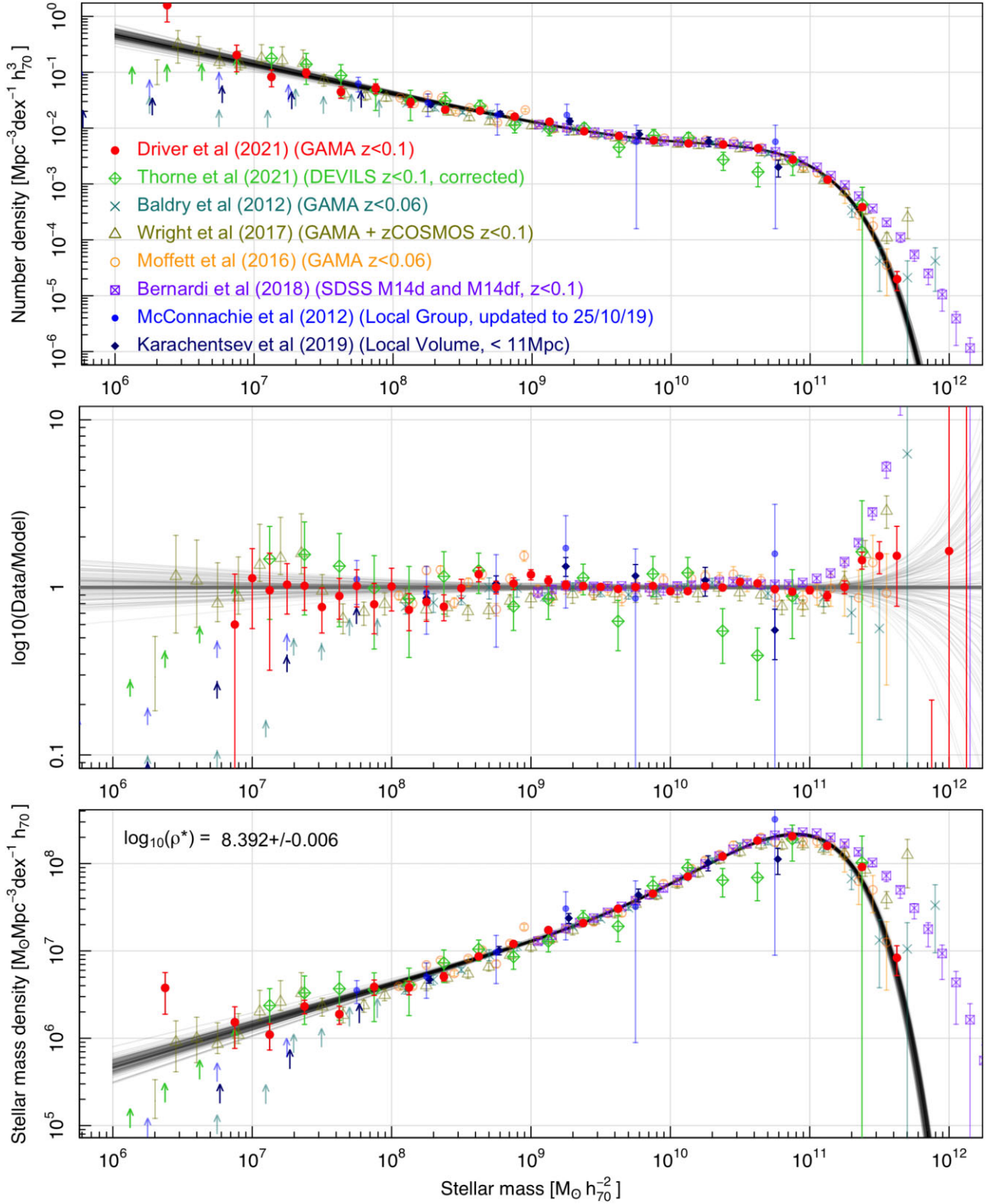
Figure 12. (Upper panel) The nearby GSMF recovered in this study and compared to recent measurements as indicated. (Centre panel) the same data but with the functional fit to the red data points (this study) removed, to highlight discrepancies relative to the quoted errorbars. The grey lines show fits to the data points when randomly perturbed by their individual errors. (Lower panel) The contribution of each stellar mass interval to the total stellar mass density. The distribution appears well bounded at high and low stellar masses suggesting the majority of the stellar mass has been identified.

$10^{6.75}$ M$_\odot$ h_{70}^{-2}. This is consistent with basic Jeans' mass arguments that, in a Cold Dark Matter dominated Universe, the lowest mass system able to collapse rather than dissipate, should be around $10^{4.5}$ M$_\odot$ h_{70}^{-2} (assuming the baryonic mass is fully converted to stars). Hence, we are gradually encroaching upon this limit, but are still just over two orders of magnitude away.

It is worth noting that the mass function is significantly less steep ($\alpha_2 = -1.53 \pm 0.03$, see Table 7) than the theoretical halo mass function ($\alpha = -1.8$), and various studies have argued that this decrease in the stellar mass to dark matter ratio, may be due to the role of supernova feedback or stellar winds ejecting baryonic mass as well as shutting down star formation in a mass-dependent manner (see review of this topic by Wechsler & Tinker 2018). An interesting side is that for this mechanism to work, star formation must occur in order to generate the SN and AGB winds. This mechanism would therefore suggest that *every* dark matter halo should contain some residual stellar mass from this initial burst of star formation, albeit potentially extended and diffuse.

This may eventually create a significant problem, as for stellar feedback (SN and Winds) to be the sole mechanisms responsible for the discrepant slopes (HMF v GSMF), we eventually require an extreme number of very low stellar mass galaxies residing in intermediate mass haloes, i.e. with exceptionally high dark matter to stellar mass ratios. While some very low mass systems do contain very high mass-to-light ratios (e.g. Battaglia et al. 2013), it is unclear whether these are fully representative of all low mass haloes. The obvious solutions are that these extreme systems are of exceptionally low surface brightness and rendered undetectable, that some other process prevents stars from ever forming in lower mass haloes (i.e. a failure to spark; Bullock et al. 2000), or that some external process prevents the gas collapsing (Benítez-Llambay et al. 2017). A viable example might be the ambient radiation field that a higher mass galaxy exerts on the surrounding environment to prevent the cooling of gas in nearby less massive haloes. At present, while we are finding relatively small numbers of very dark matter dominated systems, these are typically restricted to rich cluster environments, thus far. Similarly, 21-cm studies have yet to identify strong cases of neutral gas only systems which cannot be explained as ejected mass from a nearby companion.

From integrating our GSMF to $10^{6.75}$ M$_\odot$ h_{70}^{-2}, we find a space density of 0.24 ± 0.04 galaxies per Mpc$^3 h_{70}^{-3}$. This same density of dark matter haloes is reached for a standard Halo Mass Function (HMF, see Murray et al. 2013) at a dark matter integration limit of $\sim 10^{9.6}$ M$_\odot$ h_{70}^{-2}. This implies that our lowest mass systems must have dark matter to stellar mass ratios above 700, to reconcile our GSMF with a standard ΛCDM HMF without recourse to fully dark haloes above $\sim 10^{9.6}$ M$_\odot$ h_{70}^{-2}. While high, this is not entirely inconsistent with measurements of some nearby, albeit lower mass, dwarf systems, e.g. Segue 1 with 99.9 per cent dark matter, Simon et al. (2011), and consistent with the conclusions of the simulations community summarized in Wechsler & Tinker (2018; see their fig. 2).

As well as exploring the stellar mass distribution, it is also worth reviewing the total stellar mass density derived from integrating our stellar mass density function (i.e. Fig. 12 upper panel). Fig. 12 (lower panel) shows the same data but multiplied through by the abscissa to make clear the contribution of each stellar mass interval to the total stellar mass density. Here, we see that the peak is relatively narrow and centred around $10^{10.8}$ M$_\odot$ h_{70}^{-2} highlighting how M_*-galaxies dominate the contribution to the stellar mass density. We find that 90 per cent of the stellar mass lies in the range from $10^{9.6}$ M$_\odot$ h_{70}^{-2} to $10^{11.6}$ M$_\odot$ h_{70}^{-2}. The distribution drops more steeply towards higher masses, indicating a minimal (<1 per cent) stellar

mass contribution from supermassive galaxies ($>10^{11.6}$ M$_\odot$ h_{70}^{-2}), and drops more gradually towards lower stellar masses. Nevertheless, the contribution of each mass interval to the total stellar mass density has dropped by a factor of 100 from the peak to our limiting stellar mass of $10^{6.75}$ M$_\odot$ h_{70}^{-2}. This informs us that while the most numerous galaxy per decade of stellar mass has a stellar mass below $10^{6.75}$ M$_\odot$ h_{70}^{-2}, its contribution to the total stellar mass density is likely to be minimal (~ 1 per cent from a simple extrapolation from $10^{6.5}$ M$_\odot$ h_{70}^{-2} to 0 M$_\odot$ h_{70}^{-2}).

Here, we can report that by integrating the contribution to the stellar mass density, we recover a value of $\rho_* = (2.47 \pm 0.04) \times 10^8$ M$_\odot$ Mpc^{-3} h_{70} for a 737 cosmology. This equates to $\Omega_* = (1.81 \pm 0.03) \times 10^{-3}$ h_{70}^{-1} (also for a 737 cosmology). We note that these values are as yet uncorrected for any over/underdensity in the overall GAMA footprint, and are effectively a measurement at the median redshift of $z = 0.079$ and both of these issues will be addressed in Section 6.

Putting aside the issue of stripped stellar mass not accounted for in the integral of the GSMF, there are three caveats to our Ω_* measurement worth considering. The first is that one can never rule out a dramatic upturn to the distribution below our mass-limit ($10^{6.75}$ M$_\odot$ h_{70}^{-2}), e.g. a high space density of free-floating globular cluster-like mass systems at 10^6 M$_\odot$ h_{70}^{-2}. While this would appear unphysical, it is not impossible, but not supported by any observation or simulation. The second is whether our sample is missing low surface brightness systems. Without deeper data, this is always hard to assess, but we do note that the extensive search for low surface brightness galaxies in 200 deg^2 of the Hyper Suprime-Cam Survey by Greco et al. (2018), identified no low surface brightness galaxies above the GAMA magnitude limit ($r_{\mathrm{KiDSDR4}} < 19.65$ mag). The third is a fairly subtle effect related to the first caveat. Its basis is that the galaxy population shows a significant diversity of form (faint-end slopes). Hence, a valid question is whether the total stellar mass density should be derived from the extrapolation of the total distribution, or the extrapolations of the distinct morphological types. For example, in earlier studies of the GAMA morphological mass functions, extending down to 10^9 M$_\odot$ h_{70}^{-2}, Moffett et al. (2016) identified divergent slopes to some particular types, the extrapolation of which would lead to an infinite stellar mass density. We now reconsider this notion by deriving the GSMFs for each morphological class.

5.2 The morphological galaxy stellar mass functions at $z < 0.08$

We repeat the process of the previous section except for two changes. First, we extract morphological sub-samples as either: (E+HE), cBD, dBD, D, C, or H, see Section 3.5, and secondly, we elect to fit a simpler single Schechter function given by

$$\phi(M)\mathrm{d}M = \phi^* e^{-M/M^*} \left(\frac{M}{M^*} \right)^\alpha \mathrm{d}M. \tag{3}$$

As before, the three fitted parameters are defined by a characteristic mass, M*, a characteristic normalization, ϕ^*, and the faint-end slope, α.

To obtain the fitted parameters, we again make use of DFTOOLS and provide the selected data, errors, and selection function. To obtain the selection function, we examine the mass-to-light ratio distributions for each sub-population (see Fig. 13 left-hand panel) and determine the point at which the mass-to-light ratio encloses 95 per cent of that population. These mass-to-light values are then combined with the r-band flux limit ($r_{\mathrm{KiDSDR4}} < 19.65$ mag), to derive the selection functions shown on Fig. 13 (right-hand panel). These curves are fitted with a Richards curve (see equation 2) and the values are reported

Table 9. Single Schechter function fits to the GSMFs for various morphological classes at $z < 0.08$, and for the full sample with redshift cuts as indicated. Note that the $\log_{10}(\phi*)$ values *DO NOT* include the renormalization to SDSS, or the correction to redshift zero (see Section 6). To apply these corrections add 0.0866 dex to both $\log_{10}(\phi*)$ values.

Data set	$\log_{10}(M*)$ ($M_\odot\,h_{70}^{-2}$)	$\log_{10}(\phi*)$ (Mpc$^{-3}\,h_{70}^3$)	α	$\log_{10}(\rho_*)$ ($M_\odot$Mpc$^{-3}\,h_{70}$)
E+HE	10.954 ± 0.028	-2.994 ± 0.025	-0.524 ± 0.037	7.906 ± 0.018
cBD	10.499 ± 0.016	-2.469 ± 0.011	$+0.003 \pm 0.039$	8.030 ± 0.011
dBD	10.513 ± 0.031	-3.065 ± 0.035	-1.264 ± 0.023	7.543 ± 0.013
D	10.436 ± 0.038	-3.332 ± 0.044	-1.569 ± 0.018	7.411 ± 0.011
H	11.435 ± 0.354	-5.423 ± 0.324	-1.412 ± 0.11	6.211 ± 0.111
C	11.170 ± 0.970	-6.419 ± 1.123	-1.978 ± 0.118	5.814 ± 0.176
SUM	–	–	–	8.400 ± 0.015
All($z < 0.10$)	10.745 ± 0.020	-2.437 ± 0.016	-0.465 ± 0.069	8.392 ± 0.006
All($z < 0.08$)	10.774 ± 0.026	-2.424 ± 0.022	-0.601 ± 0.078	8.401 ± 0.008
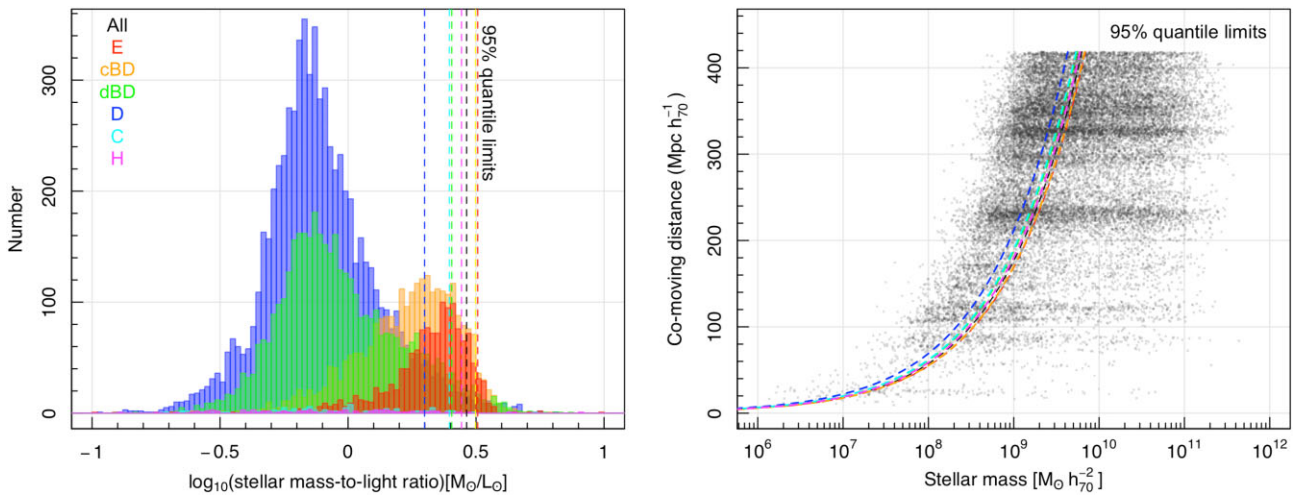
Figure 13. As for Fig. 10, except now showing the mass-to-light ratio and selection function for each morphological type as indicated.

in Table 5. These selection functions are used to select the relevant morphological sample, i.e. only those objects with masses higher than that indicated by the Richards curve are fed into the DFFIT routine to derive the morphological mass function for that class. Table s 8 and 9 shows our results. Note that in the fitting process, we need to incorporate one subtlety, which was to ensure that the fits for each of the morphological classes adopted the same underlying LSS correction. To do this, we stored the LSS correction identified from the full sample fit to $z < 0.08$ (i.e. the black curve from Fig. 14), and forced DFFIT to use this LSS solution for the subsequent fits for each morphological class.

The resulting distributions and fits are shown in Fig. 14 (upper panel), and the contribution to the stellar mass density from each morphological class is shown in the lower panel along with a pie chart representation (inset). As can be seen in Fig. 14, the summed morphological data agrees reasonably well with our earlier total estimate, i.e. $(2.51 \pm 0.05) \times 10^8\,M_\odot\,Mpc^{-3}\,h_{70}$ now versus $(2.47 \pm 0.04) \times 10^8\,M_\odot\,Mpc^{-3}\,h_{70}$ previously.

Ellipticals (red) dominate at the highest masses, followed by the cBD systems (orange), the dBD systems (green), and finally the disc only systems (blue) from $10^{9.25}\,M_\odot\,h_{70}^{-2}$ and below. The compact (gold) and hard (grey) classes contribute a small amount to the total mass density. Hence, the most frequent galaxy type is a disc, and the most massive galaxy type an Elliptical. The C and H classes start to become more significant in number at low mass, and as

the C class is nearly divergent, there is significant implied mass in its extrapolation and hence its value should be taken with great caution (as reflected in the error). The rise of the C and H classes at lower masses, also highlights the increasing difficulty in making clear classifications at our lowest mass-limit out to $z = 0.08$. Where statistics are good, the fits appear to pass through the data points well, and the single Schechter function appears to be a reasonable fit to the data.

Fig. 14 (lower panel) shows the same data but now with the mass multiplied ordinate to reflect the contribution of each type and each mass interval to the total stellar mass density. The dominant contributions come from the cBD and E classes of $(1.07 \pm 0.04) \times 10^8\,M_\odot\,Mpc^{-3}\,h_{70}$ and $(0.81 \pm 0.05) \times 10^8\,M_\odot\,Mpc^{-3}\,h_{70}$, respectively. Together, these classes make up 75 per cent of the total stellar mass density (if one ignores the mainly extrapolated C extrapolated masses).

As noted, we now obtain a total stellar mass of $(2.51 \pm 0.05) \times 10^8\,M_\odot\,Mpc^{-3}\,h_{70}$ rather than $(2.47 \pm 0.04) \times 10^8\,M_\odot\,Mpc^{-3}\,h_{70}$ from the double Schechter function fit to the full data set which is consistent within the errors.

6 THE COSMIC STELLAR MASS DENSITY

A single GAMA region, at $z < 0.1$, covers $\sim$400 000 Mpc^3 with a CV of $\sim\pm25$ per cent (see Driver & Robotham 2010, equation 3).
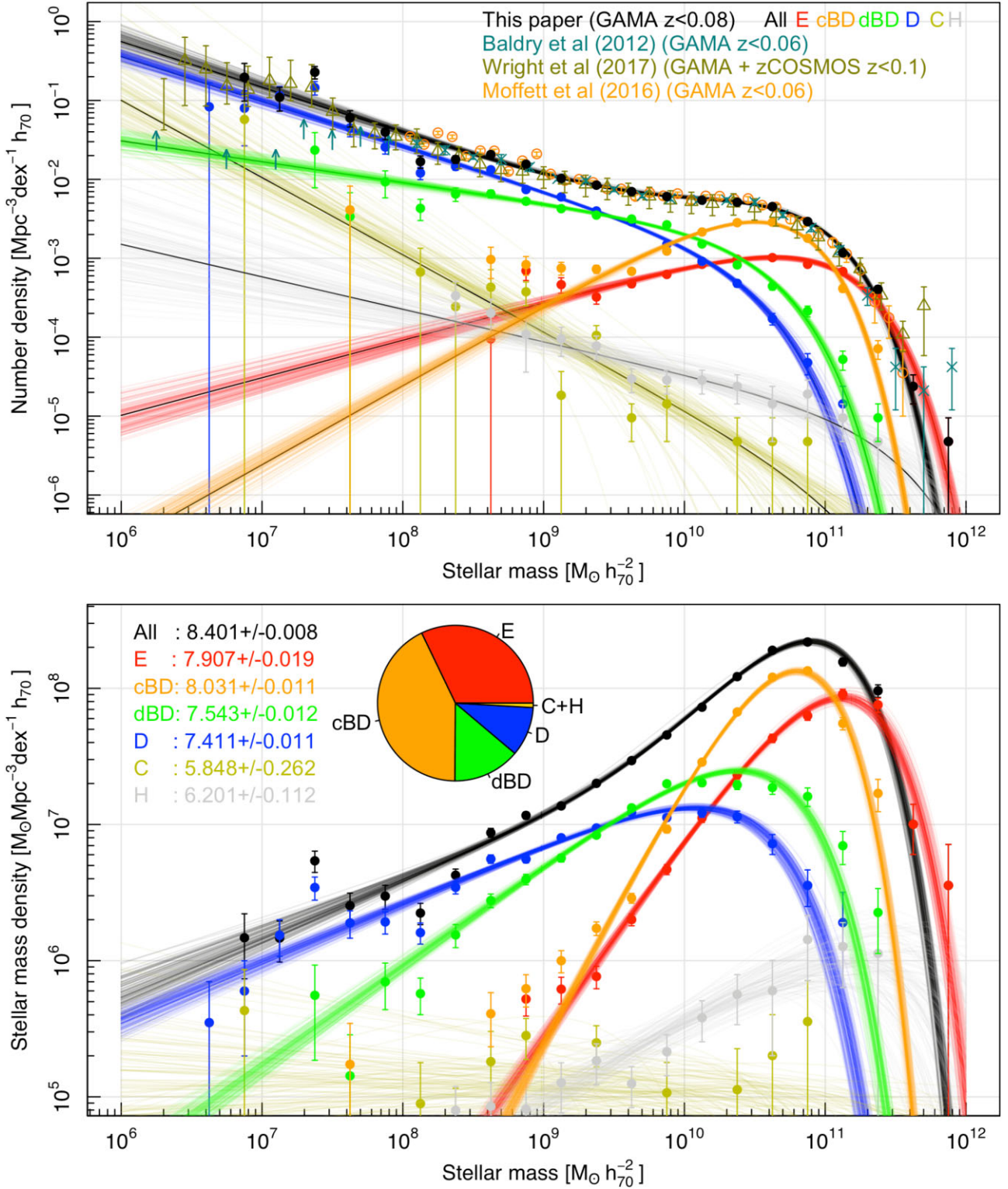
Figure 14. (Upper panel) The GSMF for various morphological types (E, red; cBD, orange; dBD, green; D, blue; C, gold; and H, grey) and compared to previous measurements. (Lower panel) the contribution of each log stellar mass interval to the overall stellar mass density. Shown as an insert is a pie diagram indicating the relative contribution of each class to the overall stellar mass density. Next to the inset are the stellar mass densities in logarithmic units from integrating the fitted mass functions (see Table 8).
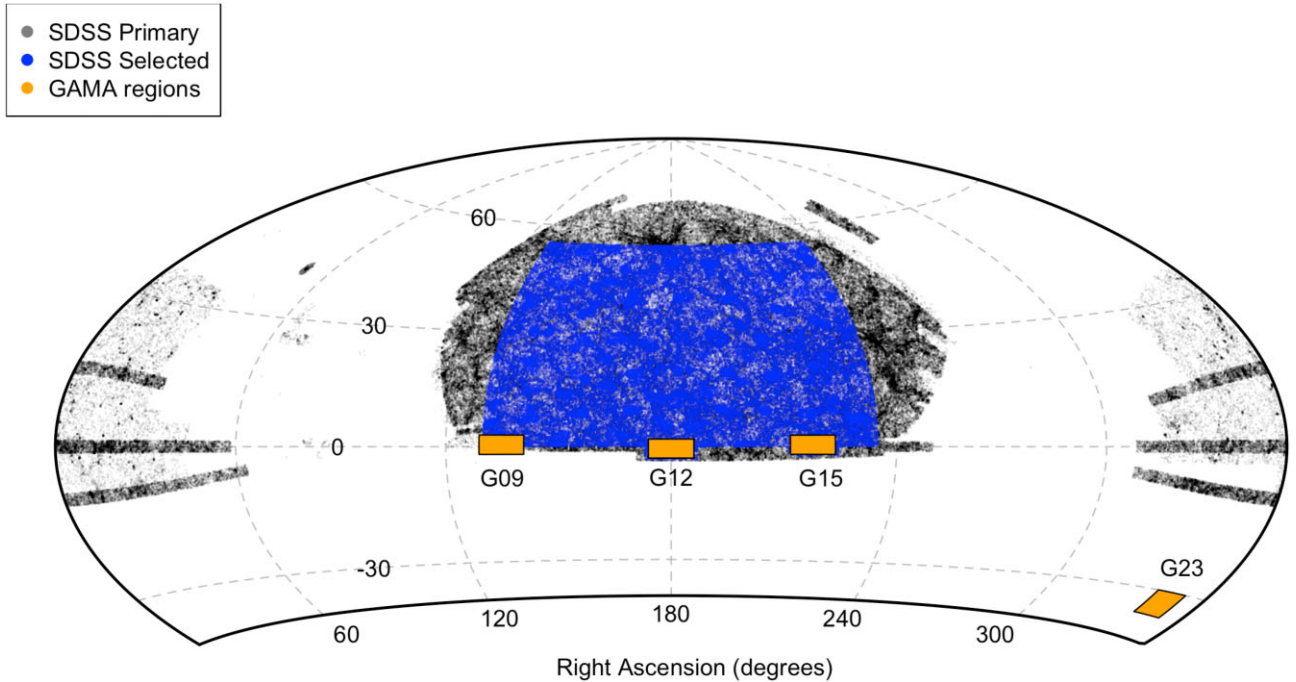
Figure 15. An Aitoff projection showing the data used for the renormalization of GAMA to SDSS. This includes the SDSS Main Survey Primary footprint (grey), the region selected for our normalization check covering 5012.134 deg^2 (blue), and the location of the GAMA fields as labelled (orange boxes).

With four fully independent sight-lines the overall CV reduces to ±12.5 per cent for the combined GAMA fields (for $z < 0.1$ measurements). This error dominates over random or formal fitting errors but can be reduced further by determining any over/underdensity relative to a wider area similar depth spectroscopic survey, with uniform characteristics, and which encompass the GAMA regions. The only suitable survey, at the present time, is the Sloan Digital Sky Survey (SDSS) which covers almost 50 times the area of GAMA and fully contains the G12 and G15 regions.

6.1 Normalization of GAMA to SDSS

Fig. 15 shows the full SDSS DR16 spectroscopic survey in grey, and the region we have selected to normalize to in blue. The four GAMA regions are shown by the four orange boxes and only G12 and G15 are fully subsumed within the SDSS spectroscopic survey footprint. Our selected SDSS region is given by $130 - 235$ in Right Ascension (deg) and $0 - 55$ in Declination (deg), plus two small extensions to cover the G12 and G15 regions fully given by: $173 - 187$ in RA and $-3.5 - 0.0$ in Dec. (G12 extension); and $210.5 - 224.5$ in RA and $-2.5 - 0.0$ in Dec. (G15 extension). This equates to a contiguous area of 5012.134 deg^2 with an estimated CV (Driver & Robotham 2010) of ±6.5 per cent. Hence, by bootstrapping to SDSS, we can theoretically rescale our results, and reduce our CV error by two times.

As only two of our regions lie within the SDSS footprint, we need to implement a double bootstrap. We first compare the density of the $z < 0.1$ (or $z < 0.08$) G12 and G15 regions to the SDSS selected area, using an SDSS tracer. We then compare the G12 and G15 regions to the full GAMA area, using a GAMA tracer. By combining the two density ratios, we can determine a normalization correction for the combined GAMA volume to the effective SDSS selected volume.

There are a number of subtleties worth highlighting. This includes an underlying implicit assumption that the SDSS completeness and

masking within the G12 and G15 regions are broadly consistent with the overall SDSS selected region. From fig. 2 of Driver & Robotham (2010), we see that this is a reasonable assumption. We also need to identify an appropriate density tracer. Previously, we and other groups have adopted an intrinsic luminosity range, and quantified the *number*-density of this tracer population between the various regions. Here, we adopt a slightly more sophisticated and stable measure. This is to use the full *r*-band luminosity density measurement by summing the intrinsic luminosities of all galaxies with $r_{\mathrm{petro}} < 17.77$ mag and $z < 0.1$ within the desired volumes.

We find that G12 and G15 combined have a density 0.8781 times that of our SDSS selected region i.e. these GAMA regions are ~12 per cent underdense. We also find, by summing the *r*-band flux of all galaxies in the GAMA regions with $r_{\mathrm{KiDSDR4}} < 19.65$ mag and $z < 0.1$ (spec-z or photo-z), that G12 and G15 are overdense compared to the combined GAMA regions by ×1.0178. Note that this estimate included consideration of the star-mask reported in Bellstedt et al. (2020a).

Hence, the overall renormalization from GAMA to SDSS selected at $z < 0.1$ is ×1.159 (and × 1.185 at $z < 0.08$). That is, we need to multiply our total GAMA density measurements by a factor of 1.159 to renormalize to an effective SDSS selected area of 5012 deg^2.

This factor is fully consistent with the estimate reported in Driver et al. (2011; see their fig. 20), and most GAMA low-z published measurements have incorporated an appropriate upward scaling. We can confirm that with the inclusion of G23, an upward scaling is still required and that overall GAMA represents a slightly underdense region of the Universe at $z < 0.1$. It is worth noting that this underdensity mainly stems from single region, G09. Hence G12, G15, and G23 can be considered reasonably representative.

Finally, we note that if we did determine the correction based on number-density rather than luminosity-density, we find a renormalization value of ×1.195 (×1.220) at $z < 0.1$ ($z < 0.08$),
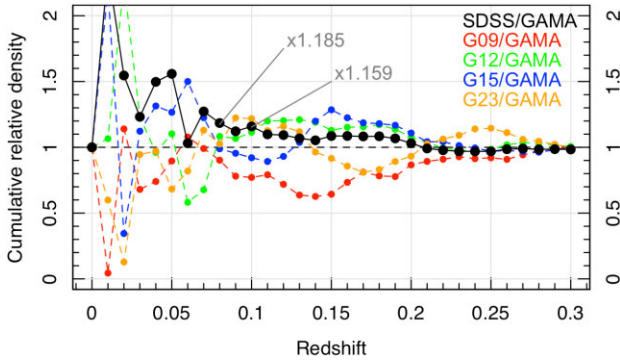
Figure 16. The cumulative density (by intrinsic flux) for GAMA compared to SDSS (black) and for each GAMA region relative to the combined GAMA area. Eventually all converge at $z = 0.3$, but at $z = 0.08$ and 0.1, we find significant multipliers are required of $\times 1.185$ and $\times 1.159$, respectively.

providing some indication of the uncertainty of the correction based on the choice of tracer.

Fig. 16 shows the same calculation as described above, but now as a function of redshift (black dots and line). The figure also shows the relative density of each GAMA field compared to the combined GAMA density (coloured dots and lines). At very low redshift, the volumes are very small and the local supercluster structure dominates. The variations then damp as the volume grows and converge to within a few per cent by $z \sim 0.3$. Noticeably, at $z \approx 0.1$, we see a range in luminosity densities of ± 14.4 per cent about the mean, which is less than the Driver & Robotham (2010) $1 - \sigma$ CV estimate of ± 25 per cent.

We have also verified that the Virgo cluster, located in the central region of the SDSS selected area, has no impact by redetermining the correction with a minimum redshift that includes or excludes the Virgo cluster (the impact is in the fifth significant figure). We note that all tables reported earlier *DO NOT* include the renormalization correction to the SDSS selected region. Hence, one can choose to adopt the results of Section 4 as GAMA unnormalized with a predicted CV error of ± 12.5 per cent, or re-scale by the factors shown in Fig. 16 to generate the GAMA normalized to SDSS values with a CV error of ± 6.5 per cent.

6.2 Evolution to a z = 0.0 CSMD measurement

One final correction, we consider is the potential for some small evolution in the stellar masses over the redshift range explored ($0 < z < 0.1$). Typically, our measurement at intermediate to high mass is weighted towards the median redshift over our full volume ($z \sim 0.079$), however, at lower masses, where volume corrections are required, the density measurement is for a progressively lower redshift range. As most galaxies are still forming stars and have existing stellar populations which are still evolving, there is the possibility of some small mass-dependent bias in our measured GSMF below $10^9 \, M_\odot \, h_{70}^{-2}$ as well as a small overall offset from $z \approx 0.079$–0.

We can estimate this effect from the recent DEVILS study by Thorne et al. (2021) who determine GSMF's from $z \approx 0.8$ to 0 and who fitted a smooth function to the total galaxy stellar mass density. This shows a net overall evolution in the cosmic stellar mass density from $z = 0.079$–0.0 of ~ 3.9 per cent. Hence, we advocate for a further correction of $\times 1.039$ to correct our final cosmic stellar mass density measurement to a $z = 0$ value of $\rho_* = (2.47 \pm 0.04)$
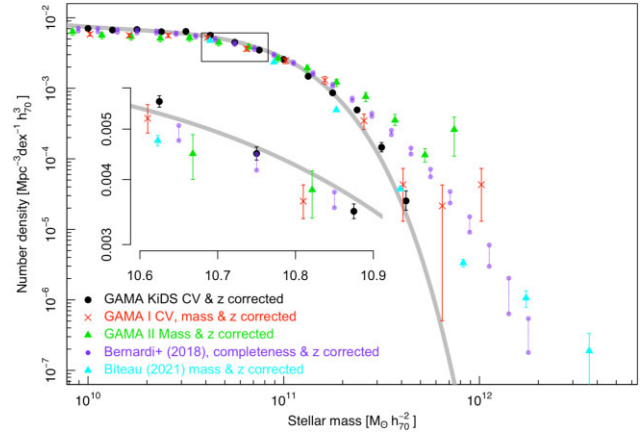
Figure 17. A comparison of recent GAMA and SDSS GSMFs around the normalization or 'knee' region, and often used to calibrate numerical simulations. The inset shows a zoom into the $M*$ region at $10^{10.75} \, M_\odot \, h_{70}^{-2}$, highlighting consistency at the 5–10 per cent level around the 'knee', but some more significant variations at the highest masses where high Sérsic indices and dense cluster cores can make photometric measurements more problematic.

$\times 10^8 \times 1.159_{\text{SDSSrenorm}} \times 1.039_{z = 0\text{correction}} \, M_\odot \, \text{Mpc}^{-3} \, h_{70}$ or $\rho_* = (2.97 \pm 0.04) \times 10^8 \, M_\odot \, \text{Mpc}^{-3} \, h_{70}$.

6.3 Comparison to earlier GAMA and SDSS DR7 GSMFs

Fig. 17 shows the 'knee' region of the GSMF for GAMA I (Baldry et al. 2012), GAMA II (Wright et al. 2017), and GAMA KiDS (this work), as well as for SDSS DR7 (Bernardi et al. 2018), and a recent local all sky compendium by Biteau (2021). A number of corrections have been made to make each data set fully consistent, and these include: mass corrections to GAMA I (+0.11 dex), GAMA II (+0.17 dex), and Biteau (2021; +0.04 dex; private communication), to the ProSpect masses used in GAMA KiDS (see Robotham et al. 2020, fig. 34), the cosmic variance correction of $\times 1.159$ for GAMA KiDS (as described above). Note that at $z < 0.06$, the CV correction for GAMA I is negligible (see Fig. 15), and for GAMA II, the methodology used a density-defining population from $0.07 < z < 0.19$ within which the CV is expected to be small.

For Bernardi et al. (2018), we implement a 11 per cent spectroscopic completeness correction. This arises from consideration of the SDSS DR7 and DR16 completeness within the G12 and G15 regions, and which suggests 87 per cent total completeness to $r_{\text{PETRO}} < 17.77$ mag, and representing all types of incompleteness including failed redshifts, fibre collisions, and the SDSS mask. As Bernardi et al. (2018) incorporated a 2 per cent correction for fibre collision incompleteness, we implement a further 1.13/1.02 per cent upward correction. Finally, all data sets are scaled to redshift zero using the value from DEVILS (see Section 6.2), of $\times 1.039$ for the $z < 0.1$ data sets (GAMA II, GAMA KiDS, SDSS DR7), $\times 1.024$ for the $z < 0.06$ data set (GAMA I and Biteau 2021), and $\times 1.030$ for the $z < 0.08$ morphological sample.

The various mass functions on Fig. 17, show good consistency around the 'knee' to within 5–10 per cent, but some significant variations at the very high mass end. This is where photometric measurements become problematic for two reasons: extended high-Sérsic index outer profiles, and blending as massive systems are often in the centres of highly crowded regions. In particular, we note that in some of our earlier works (e.g. Wright et al. 2017), we
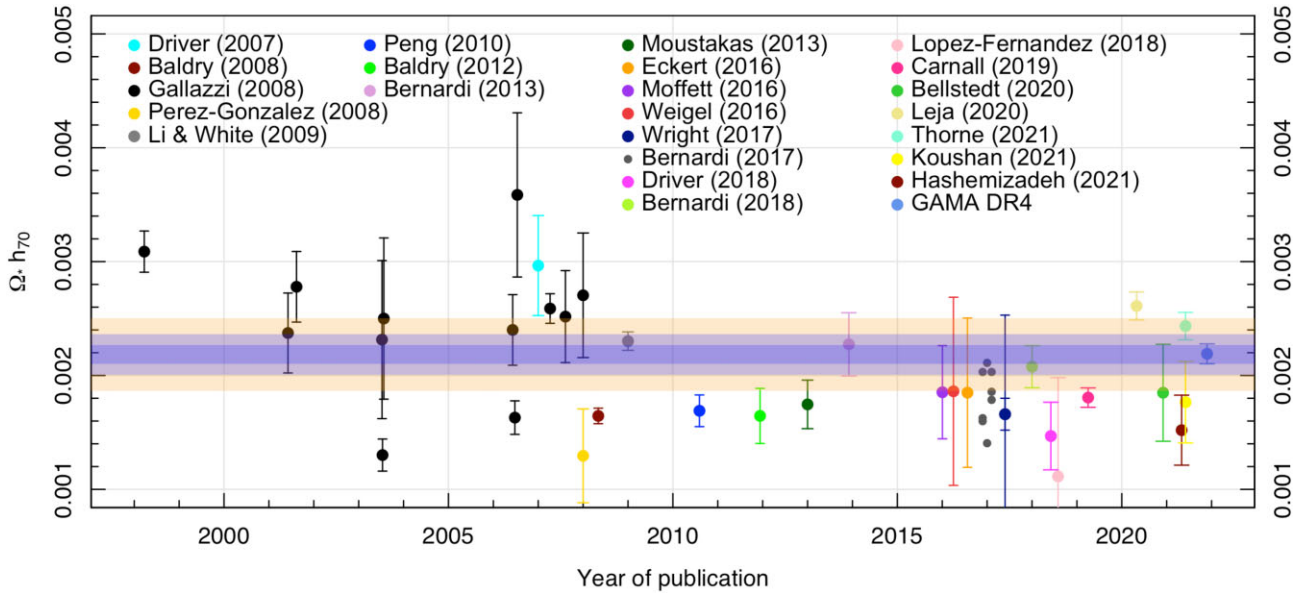
Figure 18. The galaxy stellar mass density at $z < 0.1$ as estimated by various studies (as indicated) and including the total measurement derived here (rightmost blue data point and horizontal band). The dark blue band shows the formal statistical fitting error, the light blue band shows the error including cosmic variance, and the orange band incorporating systematic uncertainties in the mass estimation and choice of IMF. All data points have been corrected to a Chabrier IMF hence the appropriate error for comparison is indicated by the fainter blue band.

used extrapolations of our Sérsic profiles to infer hidden flux, and hence mass, lurking below the isophote and outside the photometric aperture. From our deeper KiDS analysis, we can see that these corrections were in some cases excessive leading to an Eddington-like bias at the high-mass end. To ensure we have captured all of the flux for these massive systems, we visually inspected all 20 GAMA KiDS $z < 0.1$ objects above $3 \times 10^{11}\,M_\odot\,h_{70}^{-2}$ and concluded that neither photometric errors nor overblending is likely to be the case for the GAMA KiDS GSMF.

6.4 Comparison to recent measurements of Ω_*

Fig. 18 shows published estimates of the local cosmic stellar mass density (Driver et al. 2007, 2018;; Baldry, Glazebrook & Driver 2008; Pérez-González et al. 2008; Li & White 2009; Peng et al. 2010; Baldry et al. 2012; Bernardi et al. 2013; Moustakas et al. 2013; Eckert 2016; Moffett et al. 2016; Weigel, Schawinski & Bruderer 2016; Wright et al. 2017; López Fernández et al. 2018; Carnall et al. 2019; Leja et al. 2020; Bellstedt et al. 2020b; Hashemizadeh et al. 2021; Koushan et al. 2021; Thorne et al. 2021) over the past few decades, along with our new value derived from the total GSMF, renormalized to SDSS and rescaled for evolution to $z = 0$ (rightmost blue data-point). The horizontal bands highlight the error-range with the darkest blue band representing the formal fitting error, and the lighter blue band the error including the CV uncertainty following renormalization to SDSS (i.e. ± 6.5 per cent). We note that the increase between this and earlier GAMA-based measurements can be traced back to a ~ 0.06 or ~ 0.14 dex increase in our stellar mass measurements from our recent PROSPECT analysis (Bellstedt et al. 2020b) compared to earlier estimates reported in Taylor et al. (2011), or via MAGPHYS by Driver et al. (2018), respectively (with all measurements using a Chabrier IMF, see Robotham et al. 2020 for details).

We conclude that the dominant error in the measurement of the cosmic stellar mass density, is now stemming from remaining

systematic uncertainties in our stellar mass estimates, see for example, the spread of the Bernardi et al. (2017) estimates on Fig. 18 who discussed mass uncertainties due to flux, mass-to-light and dust attenuation issues (see also Sahu et al. 2019); and Hopkins (2018) who discuss mass uncertainties due to issues related to IMF uncertainty/variation. Hence, limiting depth, incompleteness, errors in redshift measurements, or statistical size (as opposed to survey volume) are no longer dominating. We also note the critical importance of the adopted underlying initial mass function (IMF). The values shown on Fig. 18 are all for a Chabrier IMF. Note that a range of IMF conversion factors are shown in Table 1 of Yu & Wang (2016) with a spread of ± 8 per cent if one excludes a pure Salpeter IMF etc (see also Madau & Dickinson 2014).

The conclusion is that the uncertainty in our measurement of the stellar mass density remains more significant than our formal errors from this analysis suggest, with random and fitting uncertainties of ~ 1 per cent, CV of ± 6.5 per cent, stellar mass estimates for a fixed IMF of ± 18 per cent, and the plausible IMF range of ± 8 per cent. In quadrature, this puts the combined error at ± 21 per cent, this uncertainty is shown as the faint orange band in Fig. 18 and indeed encompasses most previous measurements of the past decade (although we have attempted to correct all measurements plotted to a Chabrier IMF throughout).

7 SUMMARY

Through this data release, we provide full access to the Galaxy And Mass Assembly spectra, redshifts, and Data Management Units assembled over the past 12 yr by the GAMA Team. This release now includes over 230 000 new redshift measurements obtained using AAOmega on the Anglo-Australian Telescope across five regions to $r_{SDSS} < 19.8$ mag, plus a small 1 deg^2 region in which we obtain 736 redshifts (with $P(z) > 0.9$) to a fainter flux limit of $r_{SDSS} = 21.6$ mag.

As reported in Bellstedt et al. (2020a), we have now replaced the original SDSS DR6/7 photometry with new photometry based

on the significantly deeper and higher resolution ESO VST KiDS data (Kuijken et al. 2019). As this process shuffles many galaxies faintwards and some brightwards, as well as gaining and losing some galaxies, this requires us to re-evaluate our completeness limits. We now define the GAMA Main Survey to be $r_{KiDSDR4} < 19.65$ mag across the four primary regions (G09, G12, G15, G23).

The four primary regions (G09, G12, G15, G23) cover ∼230 deg^2, contain 205 540 galaxies with $r_{KiDSDR4} < 19.65$ mag, for which we have reliable redshift measurements for 195 432, i.e. 95.1 per cent complete. For the remaining galaxies for which we lack spectroscopic measurements, we obtain photometric redshift estimates via a scaled-flux matching method identical to that described in Baldry et al. (2021). We also include EAZY photometric redshift estimates for all 18 million objects in GKVINPUTCATV02.

We have morphologically classified all galaxies with a redshift below 0.08 as either Elliptical (E+HE), compact-bulge plus disc (cBD), diffuse-bulge plus disc (dBD), disc-only (D), compact (C) or hard (H). The process is conducted blindly by three classifiers and we demonstrate better than 90 per cent consistency in almost all mass and redshift bins.

In the final stages of the paper, we construct the GSMF for each region, the combined data set, and sub-divided into each morphological type. We use the Maximum Likelihood method from the DFTOOLS package and provide a selection function based on the 95th-percentile mass-to-light distribution combined with our new nominal flux limit of $r_{KiDSDR4} = 19.65$ mag. The final GSMF now reaches down to $M \sim 10^{6.75}$ M$_\odot$ h_{70}^{-2} extending over an order of magnitude beyond our previous estimates provided by Baldry et al. (2012) and Wright et al. (2017). The extension contains no surprises, and is fully consistent with the earlier extrapolation and hence leads to no significant change in the overall stellar mass density.

Hence, we conclude that the $z = 0$ Universe contains: $(2.97 \pm 0.04_{\text{random}} \pm 0.58_{\text{systematic}} \pm 0.20_{\text{CV}}) \times 10^8$ M$_\odot$ Mpc^{-3} h_{70} of stellar mass bound within the galaxy population. This value *includes* renormalization to a 5012 deg^2 region of SDSS ($\times$ 1.159), and a correction to $z = 0$ ($\times$ 1.039). However, we do not address how much stellar mass may reside in stripped mass in the intra-halo light, but note that arguments based on the extragalactic background light would suggest this must be fairly minimal (<5 per cent, see Driver et al. 2018 and Koushan et al. 2021).

Further exploration of the GSMF to lower limits will continue, with the forthcoming 4MOST Wide Area VISTA Extragalactic Survey (WAVES; Driver et al. 2019) scheduled to commence in 2023, and which should extend GSMF measurements to below 10^6 M$_\odot$ h_{70}^{-2}. As yet, the GSMF continues to rise to our detection limits and as such the most numerous galaxy type (per decade of log mass) remains to be discovered, and its properties and space density to be quantified.

DATA AVAILABILITY

The data presented in this paper are all publicly available as part of Data Release 4 of the GAMA survey. Each of the Data Management Units outlined in Tables 3 and 4 can be accessed at http://www.gama-survey.org/dr4/.

REFERENCES

Abdalla F. B., Banerji M., Lahav O., Rashkov V., 2011, MNRAS, 417, 1891
Adelman-McCarthy J. K. et al., 2008, ApJS, 175, 297
Ahn C. P. et al., 2014, ApJS, 211, 17
Ahumada R. et al., 2020, ApJS, 249, 3
Alpaslan M. et al., 2014, MNRAS, 438, 177
Amon A. et al., 2018, MNRAS, 479, 3422
Baldry I. K., Glazebrook K., Driver S. P., 2008, MNRAS, 388, 945
Baldry I. K. et al., 2010, MNRAS, 404, 86
Baldry I. K. et al., 2012, MNRAS, 421, 621
Baldry I. K. et al., 2014, MNRAS, 441, 2440
Baldry I. K. et al., 2018, MNRAS, 474, 3875
Baldry I. K., Sullivan T., Rani R., Turner S., 2021, MNRAS, 500, 1557
Battaglia G., Helmi A., Breddels M., 2013, New A Rev., 57, 52
Beeston R. A. et al., 2018, MNRAS, 479, 1077
Bellstedt S. et al., 2020a, MNRAS, 496, 3235
Bellstedt S. et al., 2020b, MNRAS, 498, 5581
Benitez N. et al., 2015, in Cenarro A. J., Figueras F., Hernández-Monteagudo
    C., Trujillo Bueno J. , Valdivielso L., eds, Proc. XI Scientific Meeting
    of the Spanish Astronomical Society, Highlights of Spanish Astrophysics
    VIII. p. 148
Benítez-Llambay A. et al., 2017, MNRAS, 465, 3913
Bernardi M., Shankar F., Hyde J. B., Mei S., Marulli F., Sheth R. K., 2010,
    MNRAS, 404, 2087
Bernardi M., Meert A., Sheth R. K., Vikram V., Huertas-Company M., Mei
    S., Shankar F., 2013, MNRAS, 436, 697
Bernardi M., Meert A., Sheth R. K., Fischer J. L., Huertas-Company M.,
    Maraston C., Shankar F., Vikram V., 2017, MNRAS, 467, 2217
Bernardi M. et al., 2018, MNRAS, 475, 757
Beutler F. et al., 2011, MNRAS, 416, 3017
Bezanson R. et al., 2011, ApJ, 737, L31
Bezanson R. et al., 2018, ApJL, 868, L36
Bilicki M. et al., 2021, A&A, 653, A82
Biteau J., 2021, ApJS, 256, 15
Blake C. et al., 2013, MNRAS, 436, 3089
Blanton M. R. et al., 2005, AJ, 129, 2562
Blanton M. R. et al., 2017, AJ, 154, 28
Bongiovanni Á. et al., 2019, A&A, 631, A9
Bourne N. et al., 2016, MNRAS, 462, 1714
Brammer G. B., van Dokkum P. G., Coppi P., 2008, ApJ, 686, 1503
Brinchmann J., Charlot S., White S. D. M., Tremonti C., Kauffmann G.,
    Heckman T., Brinkmann J., 2004, MNRAS, 351, 1151
Brough S. et al., 2013, MNRAS, 435, 2903
Brown M. J. I. et al., 2014, ApJS, 212, 18
Bruzual G., Charlot S., 2003, MNRAS, 344, 1000
Bryant J. J. et al., 2020, Proc. SPIE Conf. Ser. Vol. 8, Hector: A New Multi-
    Object Integral Field Spectrograph Instrument for the Anglo-Australian
    Telescope. SPIE, Bellingham, p. 1144715
Bullock J. S., Kravtsov A. V., Weinberg D. H., 2000, ApJ, 539, 517
Calzetti D., Armus L., Bohlin R. C., Kinney A. L., Koornneef J., Storchi-
    Bergmann T., 2000, ApJ, 533, 682
Cappellari M., 2017, MNRAS, 466, 798
Carnall A. C., Leja J., Johnson B. D., McLure R. J., Dunlop J. S., Conroy C.,
    2019, ApJ, 873, 44
Casteels K. R. V. et al., 2014, MNRAS, 445, 1157
Chabrier G., 2003, PASP, 115, 763
Cirasuolo M. et al., 2020, The Messenger, 180, 10
Cluver M. E. et al., 2014, ApJ, 782, 90
Cluver M. E. et al., 2020, ApJ, 898, 20
Colless M. et al., 2001, MNRAS, 328, 1039
Crill B. P. et al., 2020, in Lystrup M., Perrin M. D., Batalha N., Siegler N.,
    Tong E. C., eds, Proc. SPIE Conf. Ser. Vol. 11443, Space Telescopes
    and Instrumentation 2020: Optical, Infrared, and Millimeter Wave. SPIE,
    Bellingham, p. 114430I
Croom S. M. et al., 2021, MNRAS, 505, 991
da Costa L. N. et al., 1998, AJ, 116, 1

Dalton G. et al., 2020, in Evans C. J., Bryant J. J., Motohara K., eds, Proc.
    SPIE Conf. Ser. Vol. 11447, Ground-based and Airborne Instrumentation
    for Astronomy VIII. SPIE, Bellingham, p. 1144714
Davies L. J. M. et al., 2015, MNRAS, 452, 616
Davies L. J. M. et al., 2018, MNRAS, 480, 768
Dawson K. S. et al., 2013, AJ, 145, 10
de Jong J. T. A. et al., 2015, A&A, 582, A62
de Jong R. S. et al., 2019, The Messenger, 175, 3
de Lapparent V., Geller M. J., Huchra J. P., 1986, ApJ, 302, L1
De Propris R. et al., 2014, MNRAS, 444, 2200
DESI Collaboration, 2016, preprint (arXiv:1611.00036)
Drinkwater M. J. et al., 2010, MNRAS, 401, 1429
Driver S. P., Robotham A. S. G., 2010, MNRAS, 407, 2131
Driver S. P., Popescu C. C., Tuffs R. J., Liske J., Graham A. W., Allen P. D.,
    de Propris R., 2007, MNRAS, 379, 1022
Driver S. P. et al., 2009, Astron. Geophys., 50, 5.12
Driver S. P. et al., 2011, MNRAS, 413, 971
Driver S. P. et al., 2012, MNRAS, 427, 3244
Driver S. P. et al., 2016, MNRAS, 455, 3911
Driver S. P. et al., 2018, MNRAS, 475, 2891
Driver S. P. et al., 2019, The Messenger, 175, 46
Eales S. et al., 2010, PASP, 122, 499
Eardley E. et al., 2015, MNRAS, 448, 3665
Eckert K., 2016, PhD thesis, Univ. North Carolina
Edge A., Sutherland W., Kuijken K., Driver S., McMahon R., Eales S.,
    Emerson J. P., 2013, The Messenger, 154, 32
Eisenstein D. J. et al., 2011, AJ, 142, 72
Erben T. et al., 2013, MNRAS, 433, 2545
Eriksen M. et al., 2019, MNRAS, 484, 4200
Falcón-Barroso J., Sánchez-Blázquez P., Vazdekis A., Ricciardelli E., Cardiel
    N., Cenarro A. J., Gorgas J., Peletier R. F., 2011, A&A, 532, A95
Farrow D. J. et al., 2015, MNRAS, 454, 2120
Ferrarese L. et al., 2012, ApJS, 200, 4
Frieman J. A. et al., 2008, AJ, 135, 338
Gaia Collaboration, 2018, A&A, 616, A1
Geller M. J., Huchra J. P., 1989, Science, 246, 897
Geller M. J., Hwang H. S., Dell'Antonio I. P., Zahid H. J., Kurtz M. J.,
    Fabricant D. G., 2016, ApJ, 224, 11
Gordon Y. A. et al., 2017, MNRAS, 465, 2671
Greco J. P. et al., 2018, ApJ, 857, 104
Gunawardhana M. L. P. et al., 2011, MNRAS, 415, 1647
Guzzo L. et al., 2014, A&A, 566, A108
Hashemizadeh A. et al., 2021, MNRAS, 505, 136
Hopkins A. M., 2018, PASA, 35, e039
Hopkins A. M. et al., 2013, MNRAS, 430, 2047
Hotan A. W. et al., 2021, PASA, 38, e009
Huchra J., Davis M., Latham D., Tonry J., 1983, ApJS, 52, 89
Jones D. H. et al., 2004, MNRAS, 355, 747
Jones D. H. et al., 2009, MNRAS, 399, 683
Karachentsev I. D., Kaisina E. I., 2019, Astrophys. Bull., 74, 111
Kauffmann G. et al., 2003, MNRAS, 341, 33
Kelvin L. S. et al., 2012, MNRAS, 421, 1007
Kelvin L. S. et al., 2014, MNRAS, 444, 1647
Khosroshahi H. G. et al., 2017, ApJ, 842, 81
Kollmeier J. A. et al., 2017, preprint (arXiv:1711.03234)
Koushan S. et al., 2021, MNRAS, 503, 2033
Kuijken K. et al., 2019, A&A, 625, A2
Laigle C. et al., 2016, ApJS, 224, 24
Lange R. et al., 2015, MNRAS, 447, 2603
Lara-López M. A. et al., 2013, MNRAS, 434, 451
Laureijs R. et al., 2011, preprint (arXiv:1110.3193)
Lawrence A. et al., 2007, MNRAS, 379, 1599
Le Fèvre O. et al., 2005, A&A, 439, 845
Leja J., Speagle J. S., Johnson B. D., Conroy C., van Dokkum P., Franx M.,
    2020, ApJ, 893, 111
Li C., White S. D. M., 2009, MNRAS, 398, 2177
Lilly S. J. et al., 2007, ApJS, 172, 70

Liske J., Lemon D. J., Driver S. P., Cross N. J. G., Couch W. J., 2003, MNRAS, 344, 307

Liske J. et al., 2015, MNRAS, 452, 2087

López Fernández R. et al., 2018, A&A, 615, A27

Loveday J., Peterson B. A., Efstathiou G., Maddox S. J., 1992, ApJ, 390, 338

Loveday J. et al., 2012, MNRAS, 420, 1239

Loveday J. et al., 2018, MNRAS, 474, 3435

Madau P., Dickinson M., 2014, ARA&A, 52, 415

McConnachie A. W., 2012, AJ, 144, 4

McConnachie A. et al., 2016, preprint (arXiv:1606.00043)

Moffett A. J. et al., 2016, MNRAS, 462, 4336

Molino A. et al., 2014, MNRAS, 441, 2891

Moustakas J. et al., 2013, ApJ, 767, 50

Murray S. G., Power C., Robotham A. S. G., 2013, Astron. Comput., 3, 23

Newman J. A. et al., 2013, ApJS, 208, 5

Obreschkow D., Murray S. G., Robotham A. S. G., Westmeier T., 2018, MNRAS, 474, 5500

Oliva-Altamirano P. et al., 2014, MNRAS, 440, 762

Peng Y.-j. et al., 2010, ApJ, 721, 193

Pérez-González P. G. et al., 2008, ApJ, 675, 234

Planck Collaboration XI, 2014, A&A, 571, A11

Raouf M., Smith R., Khosroshahi H. G., Dariush A. A., Driver S., Ko J., Hwang H. S., 2019, ApJ, 887, 264

Raouf M. et al., 2021, ApJ, 908, 123

Ratcliffe A., Shanks T., Broadbent A., Parker Q. A., Watson F. G., Oates A. P., Fong R., Collins C. A., 1996, MNRAS, 281, L47

Robotham A. S. G. et al., 2011, MNRAS, 416, 2640

Robotham A. S. G. et al., 2014, MNRAS, 444, 3986

Robotham A. S. G., Davies L. J. M., Driver S. P., Koushan S., Taranu D. S., Casura S., Liske J., 2018, MNRAS, 476, 3137

Robotham A. S. G., Bellstedt S., Lagos C. d. P., Thorne J. E., Davies L. J., Driver S. P., Bravo M., 2020, MNRAS, 495, 905

Ruiz-Macias O. et al., 2020, Res. Notes American Astron. Soc., 4, 187

Sahu N., Graham A. W., Davis B. L., 2019, ApJ, 876, 155

Said K., Colless M., Magoulas C., Lucey J. R., Hudson M. J., 2020, MNRAS, 497, 1275

Sánchez-Blázquez P., Gorgas J., Cardiel N., González J. J., 2006, A&A, 457, 809

Shectman S. A., Landy S. D., Oemler A., Tucker D. L., Lin H., Kirshner R. P., Schechter P. L., 1996, ApJ, 470, 172

Sheth R. K. et al., 2003, ApJ, 594, 225

Simard L., Mendel J. T., Patton D. R., Ellison S. L., McConnachie A. W., 2011, ApJS, 196, 11

Simon J. D. et al., 2011, ApJ, 733, 46

Spurio Mancini A. et al., 2019, MNRAS, 490, 2155

Stoughton C. et al., 2002, AJ, 123, 485

Strauss M. A. et al., 2002, AJ, 124, 1810

Taylor E. N., Franx M., Brinchmann J., van der Wel A., van Dokkum P. G., 2010, ApJ, 722, 1

Taylor E. N. et al., 2011, MNRAS, 418, 1587

Taylor E. N. et al., 2020, MNRAS, 499, 2896

Thomas D. et al., 2013, MNRAS, 431, 1383

Thorne J. E. et al., 2021, MNRAS, 505, 540

Tingay S. J. et al., 2013, PASA, 30, e007

Tremonti C. A. et al., 2004, ApJ, 613, 898

van Uitert E. et al., 2018, MNRAS, 476, 4662

Vettolani G. et al., 1997, A&A, 325, 954

Wang S.-Y. et al., 2020, in Evans C. J., Bryant J. J., Motohara K., eds, Proc. SPIE Conf. Ser. Vol. 11447, Ground-based and Airborne Instrumentation for Astronomy VIII. SPIE, Bellingham, p. 114477V

Wechsler R. H., Tinker J. L., 2018, ARA&A, 56, 435

Weigel A. K., Schawinski K., Bruderer C., 2016, MNRAS, 459, 2150

Wolf C., Meisenheimer K., Rix H. W., Borch A., Dye S., Kleinheinrich M., 2003, A&A, 401, 73

Wright A. H. et al., 2016, MNRAS, 460, 765

Wright A. H. et al., 2017, MNRAS, 470, 283

Wright A. H., Driver S. P., Robotham A. S. G., 2018, MNRAS, 480, 3491

Yee H. K. C. et al., 2000, ApJS, 129, 475

York D. G. et al., 2000, AJ, 120, 1579

Yu H., Wang F. Y., 2016, ApJ, 820, 114

[1]*International Centre for Radio Astronomy Research (ICRAR), University of Western Australia, Crawley, WA 6009, Australia*

[2]*Astrophysics Research Institute, Liverpool John Moores University, 146 Brownlow Hill, Liverpool L3 5RF, UK*

[3]*Hamburger Sternwarte, Universität Hamburg, Gojenbergsweg 112, D-21029 Hamburg, Germany*

[4]*Centre for Astrophysics and Supercomputing, Swinburne University of Technology, Hawthorn, VIC 3122, Australia*

[5]*Faculty of Physics and Astronomy, Astronomical Institute (AIRUB), Ruhr University Bochum, D-44780 Bochum, Germany*

[6]*Imagen Technologies, 151 W 26th St, New York, NY 10001, USA*

[7]*School of Physics and Astronomy, University of Nottingham, University Park, Nottingham NG7 2RD, UK*

[8]*Vera C. Rubin Observatory, 950 N Cherry Ave, Tucson, AZ 85719, USA*

[9]*Sydney Astrophotonic Instrumentation Labs, School of Physics, the University of Sydney, Sydney NSW 2006, Australia*

[10]*Centre for Theoretical Physics, Polish Academy of Sciences, al. Lotnikow 32/46, PL-02-668 Warsaw, Poland*

[11]*School of Physics, University of New South Wales, NSW 2052, Australia*

[12]*Department of Physics and Astronomy, University of the Western Cape, Robert Sobukwe Road, Bellville 7535, South Africa*

[13]*Research School of Astronomy and Astrophysics, Australian National University, Canberra, ACT 2611, Australia*

[14]*Jodrell Bank Centre for Astrophysics, University of Manchester, Oxford Road, Mancheste M13 9PL, UK*

[15]*Leiden Observatory, Leiden University, PO Box 9513, NL-2300 RA Leiden, the Netherlands*

[16]*Kapetyn Astronomical Institute, University of Groningen, PO Box 800, NL-9700 AV Groningen, the Netherlands*

[17]*Cavendish Laboratory and Kavli Institute for Cosmology, University of Cambridge, Madingley Rise, Cambridge CB3 0HA, UK*

[18]*Sterrenkundig Observatorium, Universiteit Gent, Krijgslaan 281 S9, B-9000 Gent, Belgium*

[19]*FINCA, University of Turku, Vesilinnantie 5, F-20014 Turku, Finland*

[20]*School of Mathematics and Physics, The University of Queensland, Brisbane, QLD 4072, Australia*

[21]*Max-Planck-Institut für extraterrestrische Physik, Giessenbachstrasse, D-85748 Garching, Germany*

[22]*Institute for Computational Cosmology, Physics Department, University of Durham, Durham DH1 3LE, UK*

[23]*Institute for Astronomy, University of Edinburgh, Royal Observatory, Edinburgh EH9 3HJ, UK*

[24]*Netherlands eScience Centre, Science Park 140, NL-1098 XG Amsterdam, the Netherlands*

[25]*European Southern Observatory, Alonso de Cordova 3107, Casilla 19001, Santiago, Chile*

[26]*Department of Physics and Astronomy, 102 Natural Science Building, University of Louisville, Louisville KY 40292, USA*

[27]*Australian Astronomical Optics, Macquarie University, 105 Delhi Rd, North Ryde, NSW 2113, Australia*

[28]*Department of Astronomy, University of Cape Town, Rondebosch, Cape Town 7700, South Africa*

[29]*Pathways and Academic Learning Support Centre, University of Newcastle, Callaghan NSW 2308, Australia*

[30]*Department of Astrophysical Sciences, Princeton University, 4 Ivy Lane, Princeton, NJ 08544, USA*

[31]*Armagh Observatory and Planetarium, College Hill, Armagh BT61 DG, UK*

[32]*Curtin Institute for Computation, Curtin University, PO Box U 1987, Perth WA6845, Australia*

[33]*Astronomy Centre, University of Sussex, Falmer, Brighton BN1 9QH, UK*

[34]*Indian Institute of Science Education and Research Mohali - IISERM, Knowledge City, Manauli, 140306 Punjab, India*

[35]*Department of Physics and Astronomy, University of North Georgia, 3820 Mundy Mill Rd., Oakwood GA 30566, USA*

[36]*School of Physics and Astronomy, Sun Yat-sen University, Guangzhou 519082, Zhuhai Campus, PRC*

[37]*Department of Physics and Astronomy, Macquarie University, NSW 2109, Australia*

[38]*Astronomy, Astrophysics and Astrophotonics Research Centre, Macquarie University, Sydney, NSW 2109, Australia*

[39]*INAF - Osservatorio Astronomico di Padova, via dell'Osservatorio 5, I-35122 Padova, Italy*

[40]*Astrophysics Group, School of Physics, Tyndall Avenue, University of Bristol, Bristol BS8 1TL, UK*

[41]*E.A. Milne Centre for Astrophysics, University of Hull, Cottingham Road, Kingston-upon-Hull HU6 7RX, UK*

[42]*Jeremiah Horrocks Institute, School of Natural Sciences, University of Central Lancashire, Preston PR1 2HE, UK*

[43]*The Observatories of the Carnegie Institute for Science, 813 Santa Barbara Street, Pasadena, CA 91101, USA*

[44]*School of Physics and Astronomy, Queen Mary University of London, Mile End Road, London E1 4NS, UK*

[45]*Mas-Planck-Institue fuer Kernphysik, Saupfercheckweg 1, D-69117 Heidelberg, Germany*

[46]*ESO, Karl-Schwarzschild-Str. 2, D-85748 Garching bei München, Germany*

This paper has been typeset from a TEX/LATEX file prepared by the author.